Förenklad mikroplastanalys i biogödsel - möjligheter med AI

High-End Microplastic analysis in biosolids – AI's potential

Crislaine Bertoldi, Milda Pucetaite, Maria Hansson, Carl Troein, Martijn van Praagh

1 Summary

Global biogas and biomethane production reached 1.6 EJ in 2022, with Europe contributing nearly half. In Sweden, digestate from biogas plants is widely used as biofertilizer, of which over 1.8 million tons was applied to farmland in 2023. While biofertilizers help close nutrient loops and reduce reliance on synthetic fertilizers, they may also introduce contaminants, notably microplastics (<5mm). These microplastics can enter biogas plants together with the feedstock, yet their contribution to soil contamination remains poorly understood.

Microplastics (MPs) are an emerging concern, and Europe's farmland is estimated to receive 31,000–42,000 tons annually from biosolids and composts. Regulations are beginning to limit visible impurities in fertilizers (<2mm), but smaller particles are the most abundant fraction and are not yet addressed. Studies already show microplastics alter soil properties, microbial communities, and plant performance.

Existing data reveal wide variability in microplastic concentrations in biofertilizers across Europe, but for the best of our knowledge there is no study in Sweden regarding this topic. To fill this gap, we first developed a sample pre-treatment and analytical technique to find, characterize and measure microplastics in biofertilizer (part 1), and subsequently analyze biofertilizer samples from three certified Swedish biogas facilities with the following goals and results:

1. Develop an analytical protocol for microplastic analysis in biofertilizer.
   Results from this study: A combination of Fenton-reagent and enzymatic degradation with subsequent density separation and filtration resulted in workable samples, which despite residual organic matter could be analyzed both in the microscope and with spectroscopic techniques such as the traditional Raman- and FTIR-spectroscopy, but also the more advanced but less researched O-PTIR technique (see mid-term report and Bertoldi et al. (2025)).
2. Assess their role as a source of microplastics to agricultural soils.
   Results from this study: All three biofertilizers contained a large number of relatively small microplastics. Application of biofertilizer to soil adds microplastics. The same is true for sewage sludge and compost from garden waste.
3. Characterize particle size, morphology, and polymer composition.
   Results from this study: Fragments dominated (98%, n = 2,325), primarily within the 5–50 µm range (75%), suggesting consistent fragmentation and production conditions across facilities. Composition of 71% of analyzed particles was identified via O-PTIR spectroscopy and paint-derived particles were the most abundant.
4. Estimate annual microplastic inputs to Swedish farmland via biofertilizer application.
   Results from this study: A comparison between annual microplastic contamination by application of biofertilizer to agricultural soil showed it to be much smaller than the likely contribution from atmospheric deposition.
5. Investigate new options for AI-assisted microplastics characterization.
   Results from this study: The O-PTIR technique has promising features that could enable automation of certain steps in the measurement of microplastic particles in environmental samples. A previously developed machine learning model, however, failed to correctly identify particles. Specialized and extensive training on a large number of samples will be required to make full use of AI and ensure reliable results.

2 Methods

2.1 Extraction efficiency of the process

We evaluated MPs recovery using a clean control soil collected from Blæsedalen Valley, Disko Island, Greenland (sampled 27 Feb 2024). Polyethylene (PE, green rigid) and polypropylene (PP, blue

film) were chosen as test polymers, sourced from real-world plastic fragments (from composting facility). Particles were generated by wet cutting/mixing, sieved to 100–500 µm, and imaged pre-treatment (**Figures S1–S6**). For each test, twelve particles of each polymer were spiked into 1 g of soil, mixed, and subjected to the oxidation workflow in glassware. Recovery was calculated as the ratio of particles retrieved to particles added. All controls were performed in triplicate.

2.2 Pretreatment of the samples

To remove impurities, 50 mL of filtered hydrogen peroxide (H_2O_2, 35%) was added to 1 g (dry matter) of biofertilizer along with 50 mL of acidified iron sulfate solution ($FeSO_4$, 0.05 mol L^{-1}, pH 1.0). The sample was heated (~50ºC) under mild magnetic stirring for 1h. After this, the sample was filtered and transferred to an Erlenmeyer with 5 mL of cellulase blend with 25 mL of 0.1 M NaAc buffer (pH 5) incubated at 40 °C for 24 hours in an orbital shaker. After that, the sample was submitted to density separation with zinc chloride (1.4 g cm^{-3}) for 72 h and filtered in Anodisc filter (47 mm and 0.45 µm). In the end of the process, the filters were stored in glass petri dishes to dry at room temperature until the characterization. All treatments were performed in triplicate. The protocol was optimized at the start of this project and published in the Journal of Hazardous Materials as "Effects of pre-treatment on characterization of microplastics in biosolids via optical photothermal infrared spectroscopy" (Bertoldi et al., 2025).

2.3 Morphological and chemical characterization

Microplastics were classified by color (white/transparent, red/pink/orange, blue, green, black, yellow), morphology (fragment, fiber, microbead), and size (≥5–≤5000 µm). Imaging was performed on a microscope with a 10×/0.25 plan objective (Olympus CX33; Infinity 1 camera; Infinity 6.5 software). Anodisc filters were inspected using a helical transect covering six 1 cm² squares (56% of the effective area), following the approach tested and optimized in the first stage of this project (Bertoldi et al., 2025). Results are reported as items g^{-1} dry biosolid.

We identified microplastics on Anodisc filters using O-PTIR (mIRage, Photothermal Spectroscopy Corp., USA). Optical images were acquired at 10×/0.3 and 40×/0.78 (Nikon Plan Fluor). IR spectra were collected by tuning the laser from 950–1800 cm^{-1}, and data were processed in O-PTIR Studio v4.6.8838. For each sample, two square regions were imaged; a 1 × 1 cm² mosaic (9 mosaics with 35 images/mosaic, resulting in a total of 315 images) was then acquired and analyzed. **Figure 1** shows the analyzed square region for each biofertilizer sample and the number of particles analyzed per replicate. The analyzed fraction is relative to the total particle count from the helical scan. For each selected particle, ≥3 spectra were recorded. (Acquisition settings and sampling strategy were also refined during the project's first stage.)

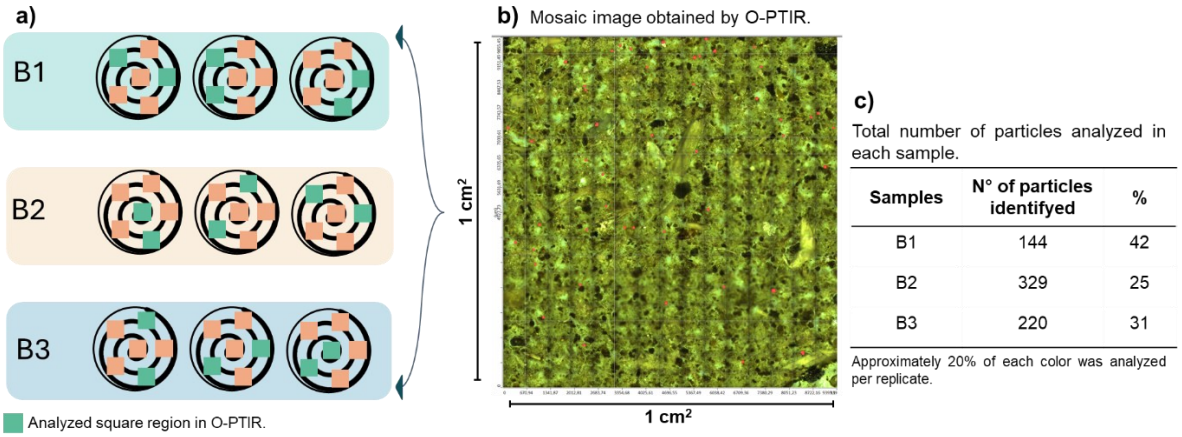

Figure 1. a) Schematic representation of the regions analyzed in each replicate of the biofertilizer sample. **b)** Mosaic images obtained by O-PTIR microscope from each of the square regions selected based on the helical count. **c)** Total number of particles analyzed in each biofertilizer sample, along with the corresponding percentage. Figure from Bertoldi et al. (2026).

2.4 Estimation of mass microplastics

We estimated microplastic mass using a modified Simon et al. (2018) protocol: (1) measure the two-dimensional area of 10 particles (5–50 µm) in ImageJ; (2) convert area to volume assuming a uniform thickness of 13 µm; (3) compute mass using polymer densities (PE = 0.95 g cm^{-3}, acrylates = 1.20 g cm^{-3}, PS = 1.05 g cm^{-3}, "other" = 1.18 g cm^{-3}); (4) average by material.

We then calculated polymer mass per m^3 and apportioned totals by material fractions (PE + PP, acrylate-based paints, PS, other identified polymers, NI treated as acrylates). Estimates were scaled to Swedish agricultural soils using the 2023 biofertilizer application (1.8 million tonnes (Avfall Sverige, 2024). Per-hectare inputs were derived by constraining application to the phosphorus (P) limit (22 kg P ha^{-1} (Bramstorp, 2014)) and our measured P concentrations (RB1: 0.6 g kg^{-1}; RB3: 0.42 g kg^{-1}).

2.5 Data analysis

We compared fiber sizes between air controls and samples with a two-sided Wilcoxon rank-sum test, reporting the Hodges–Lehmann median difference and Cliff's δ (both with 95% CIs). For fragments, size differences across color categories were tested with Kruskal–Wallis; when significant, we used Dunn's pairwise tests with Benjamini–Hochberg FDR adjustment.

For overall size patterns, we checked variance homogeneity on $\log_{10}$-transformed sizes using the Brown–Forsythe test, then tested RB1–RB3 differences with the Anderson–Darling k-sample test. Pairwise RB1, RB2, RB3 comparisons used permutation Cramér–von Mises tests with BH-adjusted p-values; effect sizes are Vargha–Delaney A12 (small ≈0.56, medium ≈0.64, large ≈0.71).

For chemically identified particles, we compared size distributions between polymers using two-sample Kolmogorov–Smirnov tests, limited to polymers with >10 particles. We controlled multiplicity with BH-FDR and highlighted pairs with FDR < 0.05 and KS distance $D \geq 0.10$. All analyses were run in RStudio 2024.12.1.

2.6 Exploring paths towards AI automation

The process of finding and characterizing microplastics through light microscopy and O-PTIR spectroscopy (section 2.3 and Bertoldi et al., 2025) is time-consuming and requires a trained and consistent expert. As neural network models have demonstrated high accuracy in classifying particles across a range of applications and spectroscopic methods (Huang, 2025), we also explore how such methods can be applied to this protocol. While a fully automated analysis workflow is desirable in practical applications, our present aim is rather to identify suitable AI models and methods that may aid further research.

A tool for particle detection is available in the O-PTIR Studio software, but it requires a clean, uniform background which the Anodics filters do not provide. Many other methods are available for finding and identifying particles in images (Huang, 2025); of particular interest is the model developed for the GEPARD project for Raman and FTIR spectroscopy (Brandt 2020; Hassellöv, 2023). As GEPARD cannot control the O-PTIR hardware, while O-PTIR Studio lacks a suitable interface for integrating such custom functionality, the initial approach is to analyze and suggest O-PTIR sampling points in exported images.

3 Results and discussion

3.1 Efficiency of the extraction procedures and recovery rates

Recovery tests yielded 126% ± 10% for PE and 76% ± 17% for PP. PE over-recovery likely reflects particle fragmentation during extraction (more blue particles with smaller sizes; **Figure 2**). In contrast, this behavior was not observed for PP, which maintained similar particle sizes after extraction. Size details are in **Table S1**; post-pretreatment images are in **Figures S7–S12**.

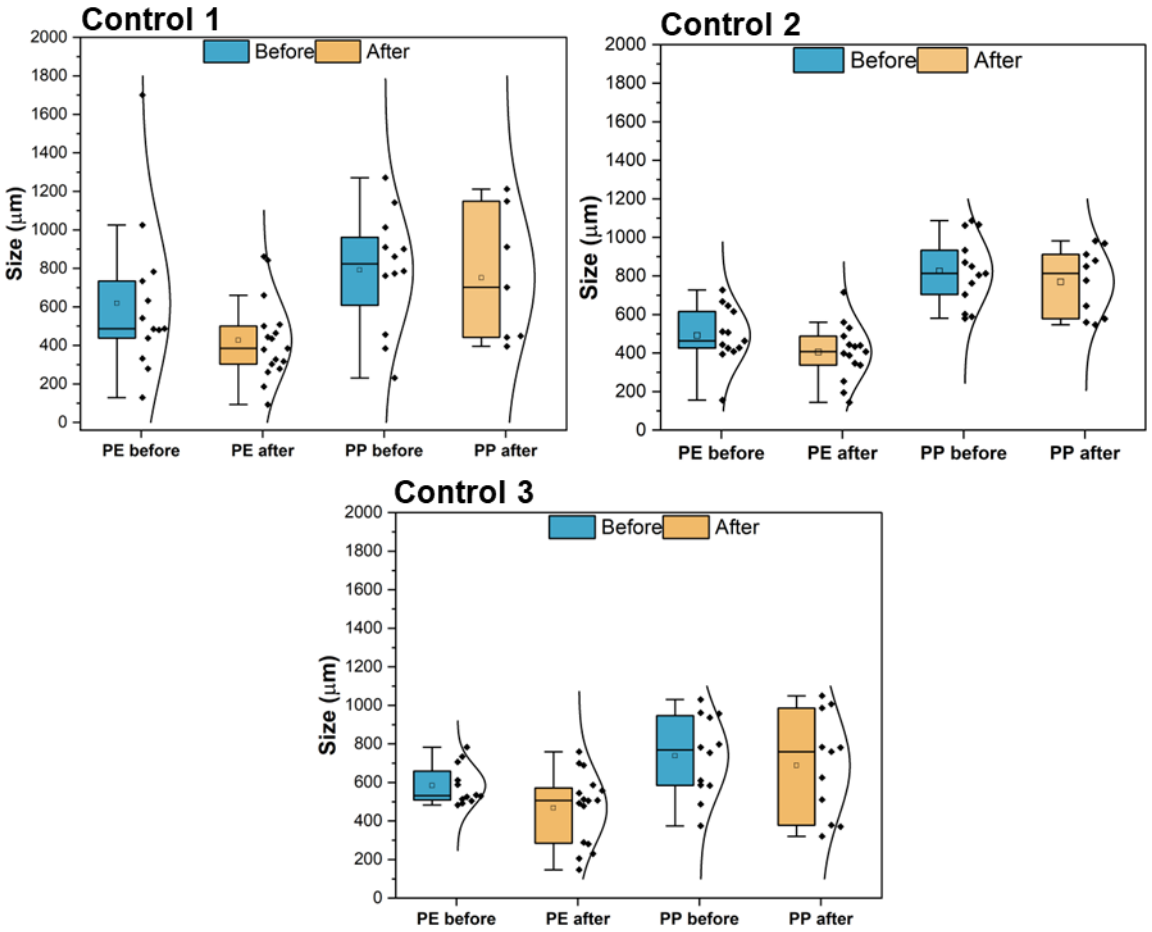

Figure 2. Size distribution of the PE and PP particles before and after the extraction treatment in the control experiment. Figure from Bertoldi et al. (2026).

3.2 Input of microplastics in soil from biofertilizer applications

Microplastic concentrations (>5 µm) ranged from 171,840 to 887,840 particles kg^{-1}: RB1 = 203,463 ± 29,755; RB2 = 784,616 ± 96,632; RB3 = 425,423 ± 199,983 (**Figure 3**). ANOVA indicated significant differences among samples (p = 0.003); Tukey's test showed RB1 differed from RB2 and RB3. Despite variability, all concentrations are the same order of magnitude.

We observed an association between feedstock composition and suspected microplastic abundance across biogas plants. As shown in Figure 3, samples with a higher share of food waste contained more microplastic particles and showed greater variability than those with less food waste.

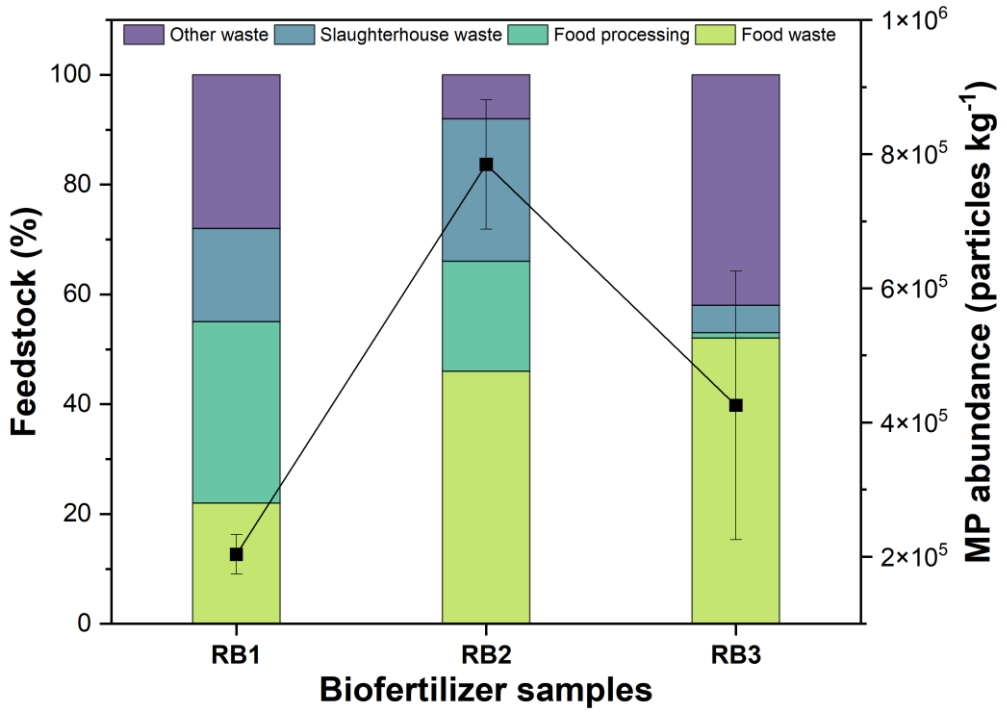

Figure 3. Feedstock types used by the biogas facilities and the corresponding microplastic abundance quantified in the current study.

Our particle counts were higher than those in prior studies. For example, Weber et al. (2025) reported 11,600 ± 660 items kg^{-1} (related to dry matter) for particles ≥20 µm, while even our lowest sample was ~20× higher. This is partly due to our lower size cutoff (≥5 µm). When we apply ≥20 µm, our values drop by ~40% but remain higher. Compared with Öling-Wärnå et al., RB1 is similar, whereas RB2 and RB3 are higher; using their ≥40 µm cutoff reduces our concentrations by ~70%, yet smaller particles still drive differences. Overall, these comparisons show that the choice of size threshold strongly affects results. Since smaller particles are most abundant, excluding them can underestimate inputs to soils.

Compared with sewage sludges, reported microplastic levels in biogas digestates are generally lower, yet our samples still exceeded values from several studies. For example, Chaudhary and Suthar (2023) reported 29,200–60,800 items kg^{-1} (≥20 µm) and Xu et al. (2020) found 2,933–5,333 items kg^{-1} (≥50 µm). Our higher counts likely reflect our lower size cutoffs. These comparisons underscore the need to include particles <40 and <20 µm in monitoring, as smaller microplastics can have stronger biological effects: earthworms accumulated more 10 µm and 1 µm particles than larger ones (Xiao et al., 2022), and small MPs (<35 µm) caused the most severe root impacts in strawberries (Cui et al., 2024).

Although size matters, relying on a single metric can bias interpretation of microplastic effects (e.g., pollutant adsorption, microbial colonization) (Ma et al., 2019; Thornton Hampton et al., 2022; Wu et al., 2025). Therefore, in addition to Feret's diameter (the longest distance across the particle), we measured particle area to show how the two metrics can diverge. For example, from our data, two particles with similar Feret's diameters (11.4 and 12.7 µm) had very different areas (14 vs. 121 $µm^2$); the second particle's area was ~8.6× larger. Thus, even at the same thickness and density, such particles would have different masses, influencing mobility, microbial interactions, sorption, and plant uptake.

Using the estimated 2023 application of ~1.8 million tonnes of biofertilizer in Sweden (Avfall Sverige, 2024), we estimate (3.81 ± 2.14) × 10^{13} microplastic particles were introduced to agricultural soils in 2023.

Per-hectare inputs averaged (8.38 ± 5.23) × 10^8 particles ha^{-1}. This enables comparison with atmospheric deposition. For example, Allen et al. (2019) reported 3.65 × 10^6 particles ha^{-1} day^{-1} (≥5 µm) in the French Pyrenees, implying that one biofertilizer application corresponds to ~230 ± 143 days of fallout. Similarly, Xu et al. (2024) estimated 1.39 × 10^7 particles ha^{-1} day^{-1} (≥45 µm) in Hangzhou, China, indicating ~60 ± 40 days of airborne deposition for a single application.

Using particle mass estimates, microplastic concentrations in biofertilizer ranged from 0.05 ± 0.01 to 0.13 ± 0.01 mg kg^{-1} (dry weight). These values are much lower than Adhikari et al. (2024), who reported 110 mg kg^{-1} in sewage sludge biosolids (12,200 particles kg^{-1} dry). However, microplastics can accumulate in soil with repeated applications (Heinze et al., 2024). Per-hectare inputs, accounting for sample-specific phosphorus concentrations, ranged from 1.9 ± 0.28 to 9.9 ± 1.22 g ha^{-1}. Nationally, total annual inputs were estimated at 111 ± 14 to 393 ± 42 kg yr^{-1}.

3.3 Morphological and chemical profile across samples

3.3.1 Morphological distribution across samples

Only fibers were detected in air controls (**Table S2**; **Figure S13**). Across RB1–RB3, we quantified 2,372 particles: fragments dominated (98.0%, n = 2,325) and fibers were 2.0% (n = 47). Given the low fiber counts, we compared fiber sizes in samples vs. air controls. A Wilcoxon rank-sum test indicated a difference (W = 1,198, p = 0.015; n = 39 vs. 47); the Hodges–Lehmann median difference was 192 (95% CI: 40–333; units as measured), with a small effect size (Cliff's δ = 0.26). This modest difference and the presence of fibers in controls suggest possible airborne contamination. Note that controls did not undergo sample pretreatment, and their cleaner backgrounds may have improved visibility, potentially biasing size estimates.

Among fragments, size differed by color (Kruskal–Wallis $\chi^2(5) = 651$, $p = 2.22 \times 10^{-138}$; $\eta^2[H] = 0.278$). BH-adjusted pairwise Wilcoxon tests indicated: white ≈ black > yellow > green > blue > red; all adjacent contrasts were significant except white vs. black (**Table S3**). Note the small black sample (n = 17; **Table S4**), which may bias estimates. **Figure S14** shows white fragments shifted toward larger sizes and overlapping black, which is consistent with visibility bias in manual counts (larger colors are more readily detected).

This also highlights a sorting challenge of plastic materials: NIR systems used in modern facilities poorly detect black plastics because common black pigments absorb NIR, hindering spectral identification (Taneepanichskul et al., 2022). Industry should consider avoiding black plastics where alternative colors are feasible.

Overall color proportions were as follows: red 37% ± 2%, blue 28% ± 2%, green 24% ± 3%, white 6% ± 2%, yellow 3% ± 1%, and black 2% ± 1%, with broadly similar distributions across samples (**Figure 4**). A chi-square test showed only green (p = 0.006) and white (p = 0.007) differed among samples (**Table S5**). After BH–FDR correction, only RB2 vs. RB3 remained significant: green was higher in RB3 and white higher in RB2 (q = 0.0216 for both). All other pairwise contrasts were non-significant (q ≥ 0.171; **Table S6**).

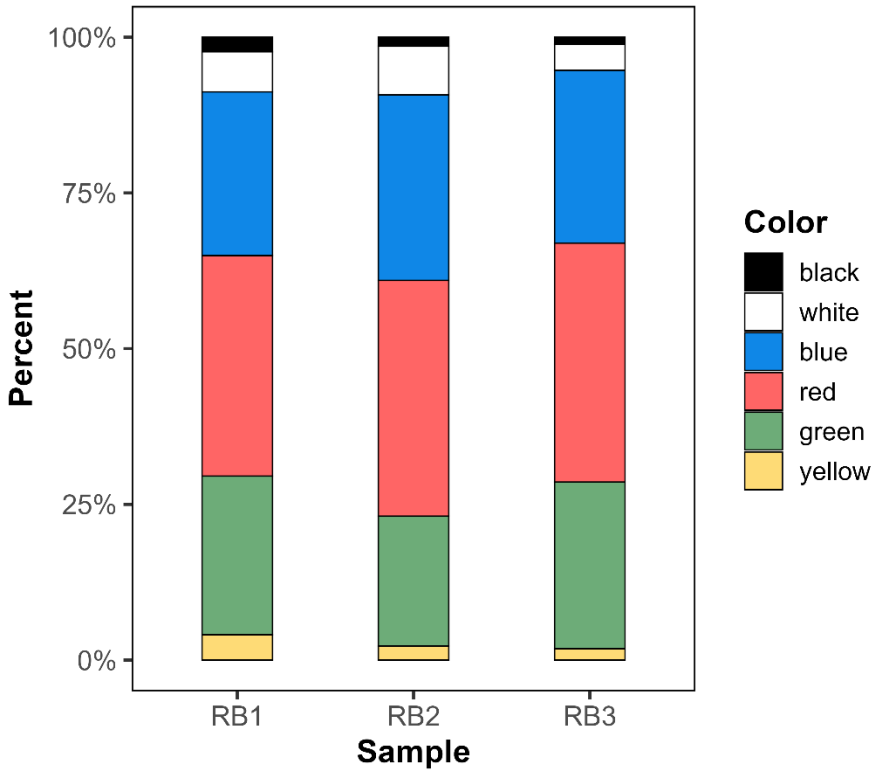

Figure 4. Color distribution of counted particles across the biofertilizer samples. Figure from Bertoldi et al. (2026).

Fragment sizes (n = 2,324; **Table S7**) showed a strong shift toward smaller particles (Figure 5). Across RB1–RB3, 98% were <500 µm, with 5–50 µm accounting for 69%, 76%, and 80% in RB1, RB2, and RB3, respectively. This pattern aligns with prior work showing higher microplastic abundance at smaller sizes (Rezaei Rashti et al., 2023).

On the $\log_{10}$ scale, the Brown–Forsythe test indicated no variance differences among samples ($F(2,2321) = 1.16$, $p = 0.313$). In contrast, Cramér–von Mises tests showed significant differences in overall size distributions; all pairwise contrasts were significant after BH–FDR ($q \leq 0.0019$; **Table S8**). Effect sizes were small for RB1–RB2 and RB1–RB3 and negligible for RB2–RB3, indicating modest differences despite statistical significance.

Figure 5b (kernel densities) shows RB1 slightly shifted toward larger sizes, with RB2 and RB3 largely overlapping. Figure 5a (rug marks) corroborates these patterns. Figure 5c (overlaid ECDFs) reinforces the shift, and Figure 5d (pairwise ECDFs with annotated KS D) localizes the largest separation to RB1 vs. RB3, with smaller gaps for RB1 vs. RB2 and RB2 vs. RB3.

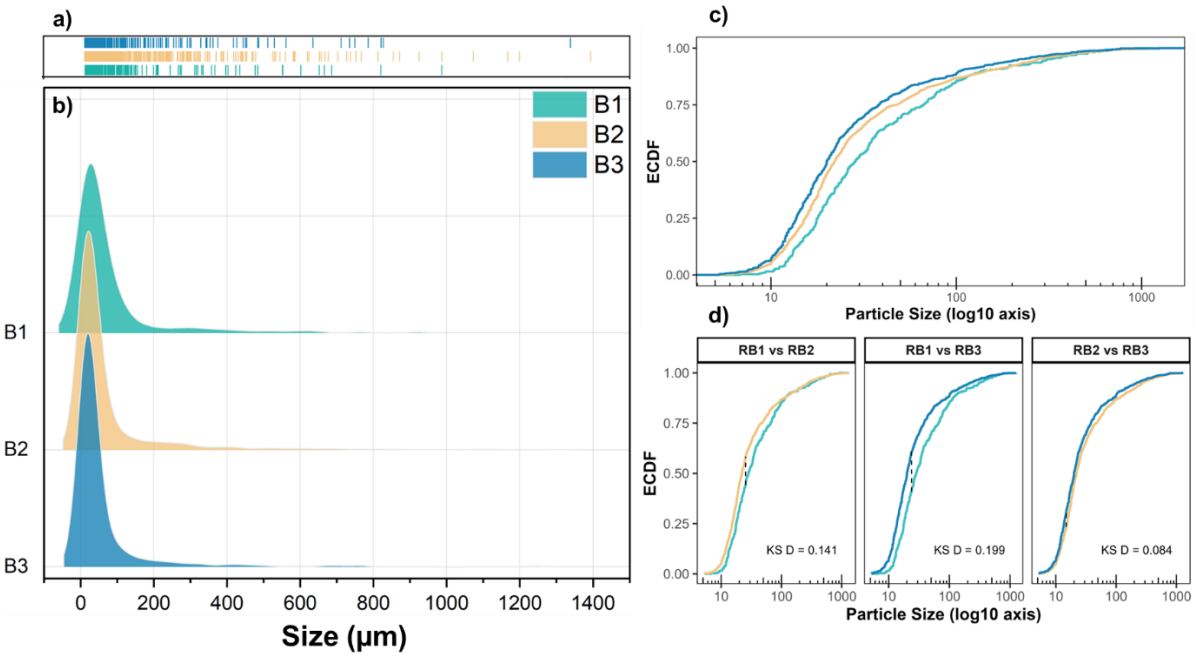

Figure 5. (a) Kernel density estimates of fragment size across samples with top rugs marking individual particles. **(b)** Overlaid empirical cumulative distribution functions (ECDFs). **(c)** Pairwise ECDFs for each sample pair, highlighting the Kolmogorov–Smirnov (KS) maximum gap: the dashed segment marks the largest vertical separation between curves, and the KS statistic DDD is annotated within each panel. Colors are consistent across panels for RB1, RB2, and RB3. Figure from Bertoldi et al. (2026).

The microplastic size distributions were consistent across the biofertilizer samples, likely reflecting standardized processing conditions at biogas plants that yield a predictable particle-size profile. This uniformity is important because it suggests that biofertilizers produced under similar operating conditions may deliver comparably sized particles to soils. Mechanical stresses inherent to treatment-shear, pressure, and turbulence—drive repeated collisions and surface abrasion, promoting fragmentation of larger plastics into smaller pieces (Monira et al., 2023). As a result, the prevalence of smaller particles in our samples is expected and aligns with observed trends in comparable systems (Letwin et al., 2024). These mechanisms offer a possible explanation for the predominance of fine particles and support the overall consistency in the size distributions we observed.

3.3.2 Polymer composition across samples

Approximately 30% of the counted particles (n = 693) were analyzed by O-PTIR, and 29% of these could not be chemically identified. Among the identified microplastics, paint-based particles were most common (23%), followed by polyethylene (12%), polystyrene (9%), polypropylene (7%), polyurethane (6%), and polyester (3%) (**Figure 6a)**. We also detected non-plastic materials such as cotton and cellulose. The full composition for each sample is provided in Table S9.

Size distributions differed modestly by polymer (Kruskal–Wallis H = 39.735, p = 0.0023, ε^2 = 0.032). As shown in **Figure 6b**, each polymer displays a distinct violin-plot profile. Pairwise Kolmogorov–Smirnov tests (**Figure 6c**) showed that 5 of 45 comparisons remained significant after FDR correction, indicating a limited set of polymers with clearly distinct size patterns. Notably, PET differed most from the others.

We compared non-identified (NI) particles with identified ones, restricting NI to those with similar spectra quality, color, and shape. Violin and density plots (**Figure 6d**) show comparable size distributions, and a K–S test found no difference (D = 0.043, p = 0.955). This suggests many NI particles are likely microplastics; non-identification may reflect surface impurities that interfered with spectroscopy.

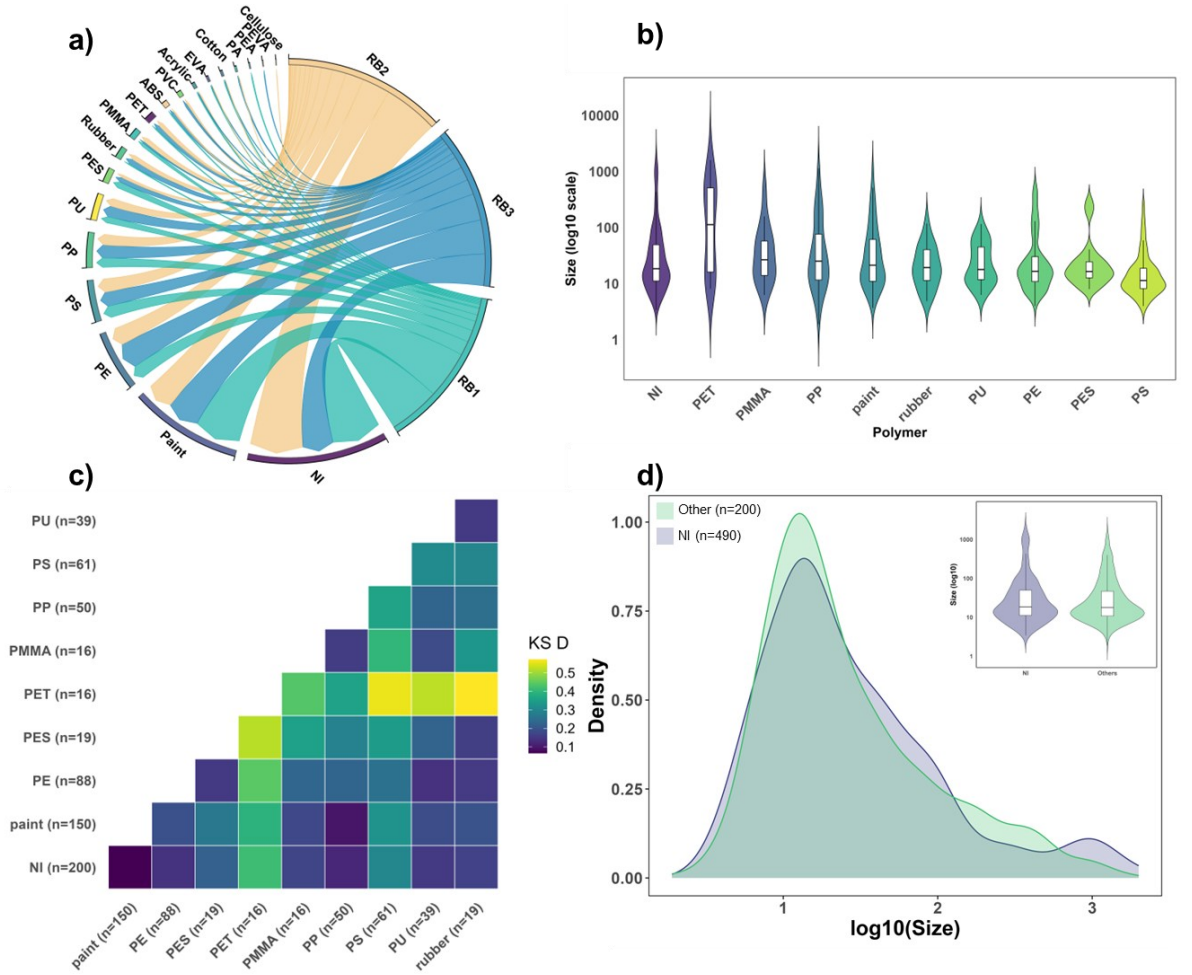

Figure 6 (a) Chord diagram showing polymer composition across samples. **(b)** Violin plots of particle size (Feret's diameter) by polymer for chemically identified particles. **(c)** Heatmap of pairwise size-distribution comparisons among chemically identified polymers (Kolmogorov–Smirnov distance; FDR-adjusted significance indicated). **(d)** Violin and kernel density plots comparing size distributions of chemically identified versus non-identified (NI) particles. Figure from Bertoldi et al. (2026).

The color distribution varied by polymer (**Figure 7a**). A Pearson chi-square test indicated a non-independent relationship between polymer and color ($\chi^2_{(45)} = 183.68$, $p = 1.14 \times 10^{-18}$; Cramér's V = 0.235; N = 665), consistent with a small-to-moderate association. The clustered heat map (**Figure 7b**) shows coherent groupings: polystyrene clusters with paint and polyethylene (relatively higher red fractions), polypropylene with PET and polyester (larger shares of white), and PMMA with rubber (greater contributions from green). These patterns suggest polymer-specific color profiles that may reflect source materials or processing histories.

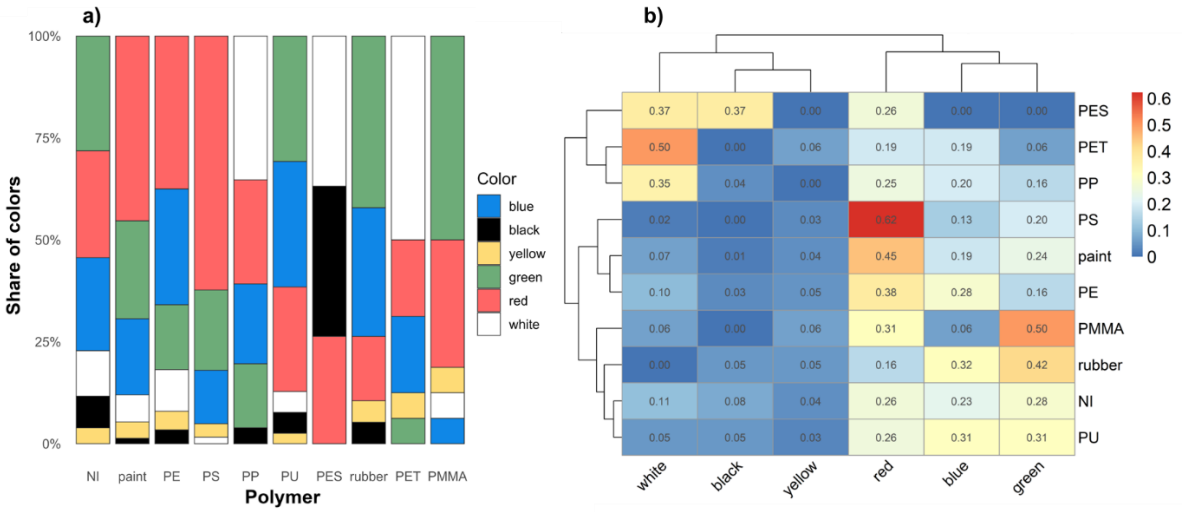

Figure 7. (**a**) 100% stacked bar chart showing the proportion of blue, black, yellow, green, red, and white items within each polymer (polymers with total n<10 were excluded). (**b**) Heat map of within-polymer composition (rows sum to 1), with numbers indicating cell percentages. Rows (polymers) and columns (colors) are ordered by hierarchical clustering (Euclidean distance, complete linkage) to highlight groups with similar color profiles. Figure from Bertoldi et al. (2026).

As noted above, paint-derived microplastics were abundant, and IR spectra indicated substantial compositional variability among paint fragments. **Figure 8** illustrates particles with distinct IR profiles, consistent with differing chemistries. This heterogeneity reflects the complexity of paint formulations and complicates impact assessment. The synthetic polymer content of paints also varies widely, which influences spectral signatures. Formulations can include polyacrylates, epoxies, polystyrene, polyurethane, polyesters, and alkyds, with the polymeric fraction ranging from approximately 10% to 90% (Oertel et al., 2025; Thuan et al., 2025). The challenges in paint identification have been emphasized by other authors, and the environmental occurrence of paint particles is considered underestimated (Diana et al., 2025). Moreover, beyond complex polymer matrices, paints can contain inorganic constituents such as Mg, Si, S, Cl, Ca, Ti, Fe, Cu, Zn, and Ba, which may heighten the environmental and biological risks associated with these particles (Kim et al., 2025).

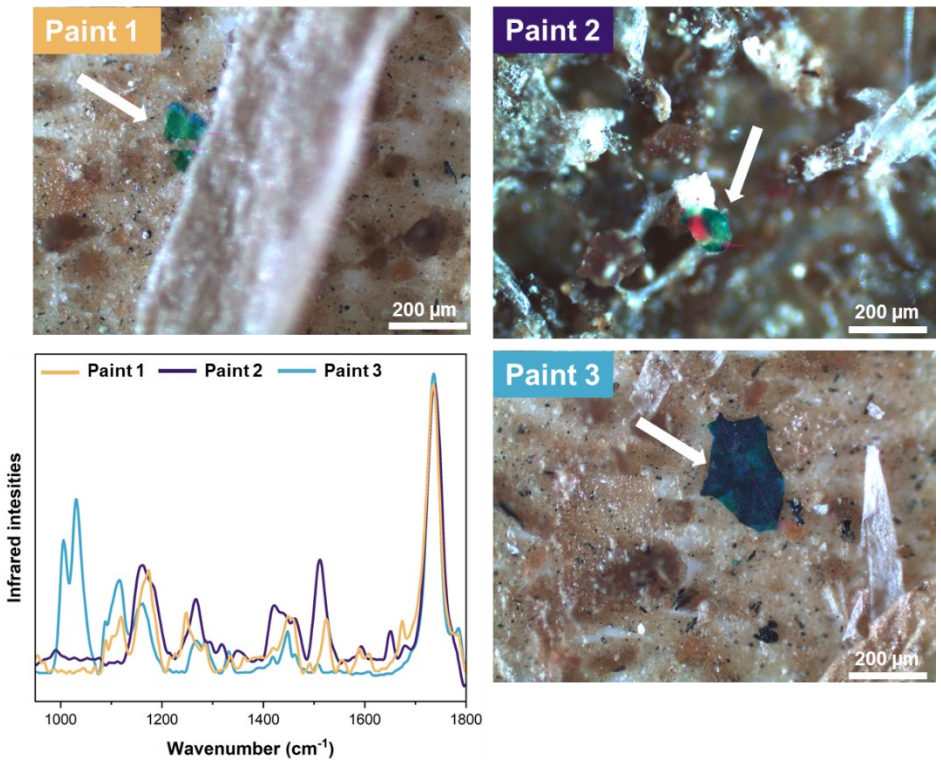

Figure 8. IR spectra of paint-based microplastics identified in the samples. Figure from Bertoldi et al. (2026).

3.4 Pyr-GC/MS analysis

Although the analytical procedure and strength of Pyro-GC/MS have been developed since the conception of this project, still its relatively high limits of quantification are a drawback for environmental samples. If the environmental matrix allows, as is often the case for water samples from which microplastic particles can be filtered through huge sample volumes, concentrations can be enhanced beyond the limit of quantification. In the case of solid samples or slurry samples as is the case with biofertilizer, this is not feasible, as miscellaneous solids also accumulate and counteract the possibility of quantifying microplastics (Pyro GC-MS also has a limit for the total organic content win the samples). After an intense and prolonged discussion with experts on Pyro GC-MS, we came to the conclusion that a pooling of our samples might lead to microplastic concentrations of the main occurring polymers above the quantification limit of Pyro-GC/MS (but it is not assured). Therefore, we intend to pool samples with the highest calculated polymer concentrations and subject them to a Pyro-GC/MS analysis. We have put these analyses on hold, however, because the method is destructive, e.g. the samples are lost forever after the analysis, and due to the low concentrations in the sample, we have to use all of the samples in order to have a fair chance to retrieve reliable results. Therefore, we want to first complete all non-destructive measurements, finalize this study and an addtional study on the effects of microplastics on soil organisms, and submit the manuscript. After acceptance of the manuscript and completion of all follow-up experimental work, we plan to perform Py-GC/MS on the samples used for the scientific publication to ensure maximum comparability. The report will be updated with these results once follow-up work is completed and manuscripts are accepted.

3.5 Limitations and future directions

This study has limitations that should be considered when interpreting the findings. Although the sample size was small—three biofertilizers from different biogas plants—it provides a robust initial assessment of microplastics in Swedish biofertilizers. The high degree of standardization in Swedish biogas operations enhances comparability across sites, and the consistent particle distributions,

abundances, and characteristics observed support the reliability of the results. While a larger and more diverse sample set would strengthen statistical inference and improve generalizability to systems with different feedstocks or processes, the present work establishes a solid, representative baseline and a clear framework for scaling up future studies on microplastics in biofertilizers from biogas facilities.

Many microplastic studies report only particle counts, which are informative but can bias or obscure estimates of environmental load. To provide a more realistic assessment, we complemented counts with mass-based estimates by converting measured particle areas to volumes using a literature-based thickness assumption. We recognize that this assumption introduces uncertainty and may affect absolute masses; however, it provides a transparent, order-of-magnitude constraint that counts alone cannot offer. Together, these approaches yield both count- and mass-based perspectives, providing a more decision-relevant baseline for regulators and underscoring the need to quantify plastic mass inputs to agricultural soils from biofertilizers produced at biogas facilities.

4 Conclusions

Our control experiments demonstrated that pretreatment can fragment microplastics, thereby inflating particle counts in real samples. This effect was particularly evident for PE, which showed apparent recoveries of 126% ± 10%. These findings highlight the importance of combining particle counts with mass-based estimates to achieve more robust assessments.

The study confirmed that biofertilizers from biogas plants represent a measurable source of microplastics to Swedish agricultural soils. All analyzed samples contained substantial concentrations, ranging from 171,840 to 887,840 particles kg^{-1} . Scaled to national application rates, this corresponds to inputs of 111 $\pm$ 14 to 393 $\pm$ 42 kg of microplastics annually. On a per-hectare basis, average loads reached $8.38 \times 10^8 \pm 5.23 \times 10^8$ particles, equivalent to 1.9–9.9 g ha^{-1} per application. While the overall mass input is moderate compared with other biosolids such as sewage sludge, the continuous and large-scale use of biofertilizers might result in a persistent microplastic influx to soils. These findings establish biofertilizers as a relevant pathway of microplastic contamination and emphasize the need for ongoing monitoring and management.

The occurrence, polymer types, morphologies, and color compositions of microplastics were broadly similar across the three biogas facilities, reflecting the high degree of standardization in Swedish biogas production. Minor quantitative differences were observed, but the overall consistency underscores the reliability of our national-scale estimates.

The dominant particles were small fragments, with 98% measuring <500 μm and 69–80% within the 5–50 μm range. This distribution was consistent across facilities and aligns with previous reports that microplastic abundance increases as particle size decreases. Paint-derived particles were most abundant (23%), followed by PE, PS, PP, PU, and PES. Although size distributions varied only modestly among polymers, PET exhibited a distinct profile, which might suggest polymer-specific fragmentation pathways. Non-identified particles displayed size distributions similar to confirmed microplastics, reinforcing the likelihood that they represent additional microplastic fractions or that all particles undergo similar size reduction. Furthermore, fragment size differed by color, with larger particles more common in white (and similar in black) compared with yellow, green, blue, and red, a pattern consistent with visibility bias in manual counting.

In summary, biofertilizers act as a measurable pathway for microplastic inputs to agricultural soils, but their agronomic and environmental benefits remain substantial. By stimulating the circular economy and recycling valuable nutrients back to soils, biofertilizers contribute to sustainable agriculture. Continued use should be coupled with monitoring and improved quality control to maximize these benefits while minimizing microplastic contamination.

4.1 AI-assisted microplastics analysis in environmental samples

Even with pretreatment, biofertilizer samples have a complex and varied appearance (see **Figure 8**), making reliable identification of microplastics a challenging task. Automation of this task is desirable, and it can be divided into two steps: identification of likely microplastics in the image, followed by acquisition and interpretation of spectra in suitable points. Some available software (e.g. O-PTIR Studio or GEPARD) can already do this for specific types of samples or specific techniques.

Image segmentation using deep convolutional neural network models (e.g. Mask R-CNN or ResNet-50) is a powerful way of identifying particles where simpler methods such as thresholding would fail. The need for labor-intensive image annotation and network training is greatly reduced by pre-trained generic models that are re-trained on a smaller set of images. Of particular interest is the Detectron2-based model used in GEPARD, as it has already been trained to segment microplastics. However, preliminary results with this model indicate that considerable retraining (using manually annotated images) will be needed because of the complex background created by the Anodisc filters (**Figure 9**).

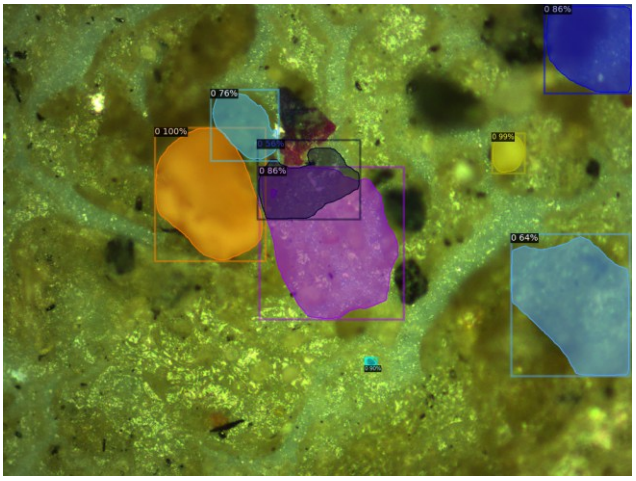

Figure 9. Example of AI segmentation to locate microplastics. Eight regions are suggested by this pre-trained model from GEPARD, but none of them include the red microplastics particle (top center). The complexity of the images will necessitate thorough re-training.

Acknowledgements

We especially thank the biogas companies that participated in the study providing samples, some data, and valuable discussions during workshops. The Greenland soil was obtained within the scope of a BECC funded project to Milda Pucetaite, and we thank the University of Copenhagen Arctic station for hosting the fieldwork. We are further grateful to Rasa Platakyte for collaboration and providing the soils used in control experiments of this work. We also thank Ola Gustafsson at the Microscopy Facility, Department of Biology, Lund University, for access to the scanning electron microscope (SEM). Finally, we thank Prof. Staffan Bensch and Jane Jönsson for providing laboratory space and access to the optical microscope.

Last but not least, the ÅForsk foundation is gratefully acknowledged for financial support of this work.

List of publications from the project

1. Bertoldi, C.; Zanke, M.; Pucetaite, M.; Hansson, M.C.; Troein, C.; Van Praagh, M. Microplastics in liquid biofertilizers: An overlooked threat to agricultural soil? Environmental Pollution **2026**, 398, 128078. https://doi.org/10.1016/j.envpol.2026.128078
2. Bertoldi, C.; Pucetaite, M.; Hansson, M. C.; Troein, C.; Van Praagh, M. Effects of Pre-Treatment on Characterization of Microplastics in Biosolids via Optical Photothermal Infrared Spectroscopy. Journal of Hazardous Materials **2025**, 496, 139448. https://doi.org/10.1016/j.jhazmat.2025.139448.
3. Amato-Lourenço, L. F.; Bertoldi, C.; Van Praagh, M.; Rillig, M. Environmental Factors Influence Airborne Microplastic Deposition in the Soil of Urban Allotment Gardens. Environmental Pollution **2025**, 375, 126372. https://doi.org/10.1016/j.envpol.2025.126372.

References

Allen, S., Allen, D., Phoenix, V.R., Le Roux, G., Durántez Jiménez, P., Simonneau, A., Binet, S., Galop, D., 2019. Atmospheric transport and deposition of microplastics in a remote mountain catchment. Nat. Geosci. 12, 339–344. https://doi.org/10.1038/s41561-019-0335-5

Avfall Sverige, 2024. Swedish Waste Management.

Bertoldi, C., Pucetaite, M., Hansson, M.C., Troein, C., Van Praagh, M., 2025. Effects of pre-treatment on characterization of microplastics in biosolids via optical photothermal infrared spectroscopy. Journal of Hazardous Materials 496, 139448. https://doi.org/10.1016/j.jhazmat.2025.139448

Bertoldi, C., Zanke, M., Pucetaite, M., Hansson, M.C., Troein, C., Van Praagh, M., 2026. Microplastics in liquid biofertilizers: An overlooked threat to agricultural soil? Environmental Pollution 398, 128078. https://doi.org/10.1016/j.envpol.2026.128078

Bramstorp, A., 2014. Regelverk som styr användningen av biogödsel. Biogödsel.

Chaudhary, M., Suthar, S., 2023. Microplastic abundance and characterization in municipal sewage sludge from cities across upper Ganga River, India: Apprising microplastic uptakes and their toxicity in the plant during sludge application in agriculture. Physics and Chemistry of the Earth, Parts A/B/C 132, 103468. https://doi.org/10.1016/j.pce.2023.103468

Cui, L., Liang, R., Zhang, C., Zhang, R., Wang, H., Wang, X.-X., 2024. Coupling polyethylene microplastics with other pollutants: Exploring their combined effects on plant health and technologies for mitigating toxicity. Science of The Total Environment 955, 176657. https://doi.org/10.1016/j.scitotenv.2024.176657

Diana, Z.T., Chen, Y., Rochman, C.M., 2025. Paint: a ubiquitous yet disregarded piece of the microplastics puzzle. Environmental Toxicology and Chemistry 44, 26–44. https://doi.org/10.1093/etojnl/vgae034

Kim, T., Eo, S., Shim, W.J., Kim, M., 2025. Characterization of ship paint-derived microplastics by Fourier transform infrared spectroscopy (FTIR), energy dispersive X-ray spectroscopy (EDS), and density analyses. Journal of Hazardous Materials 498, 139790. https://doi.org/10.1016/j.jhazmat.2025.139790

Letwin, N.V., Gillespie, A.W., Ijzerman, M.M., Kudla, Y.M., Csajaghy, J.D., Prosser, R.S., 2024. Characterizing the Microplastic Content of Biosolids in Southern Ontario, Canada. Enviro Toxic and Chemistry 43, 793–806. https://doi.org/10.1002/etc.5813

Ma, J., Zhao, J., Zhu, Z., Li, L., Yu, F., 2019. Effect of microplastic size on the adsorption behavior and mechanism of triclosan on polyvinyl chloride. Environmental Pollution 254, 113104. https://doi.org/10.1016/j.envpol.2019.113104

Monira, S., Roychand, R., Bhuiyan, M.A., Pramanik, B.K., 2023. Role of water shear force for microplastics fragmentation into nanoplastics. Environmental Research 237, 116916. https://doi.org/10.1016/j.envres.2023.116916

Oertel, G., Vaagen, H., Glavee-Geo, R., 2025. Identifying and managing ship paint microplastic pollution along the supply chain: a shipbuilding case study. Marine Pollution Bulletin 218, 118182. https://doi.org/10.1016/j.marpolbul.2025.118182

Öling-Wärnå, V., Åkerback, N., Engblom, S., 2023. Digestate from Biowaste and Sewage Sludge as Carriers of Microplastic into the Environment: Case Study of a Thermophilic Biogas Plant in Ostrobothnia, Finland. Water Air Soil Pollut 234, 432. https://doi.org/10.1007/s11270-023-06436-z

Rezaei Rashti, M., Hintz, J., Esfandbod, M., Bahadori, M., Lan, Z., Chen, C., 2023. Detecting microplastics in organic-rich materials and their potential risks to earthworms in agroecosystems. Waste Management 166, 96–103. https://doi.org/10.1016/j.wasman.2023.04.047

Simon, M., van Alst, N., Vollertsen, J., 2018. Quantification of microplastic mass and removal rates at wastewater treatment plants applying Focal Plane Array (FPA)-based Fourier Transform Infrared (FT-IR) imaging. Water Research 142, 1–9. https://doi.org/10.1016/j.watres.2018.05.019

Taneepanichskul, N., Purkiss, D., Miodownik, M., 2022. A Review of Sorting and Separating Technologies Suitable for Compostable and Biodegradable Plastic Packaging. Front. Sustain. 3. https://doi.org/10.3389/frsus.2022.901885

Thornton Hampton, L.M., Brander, S.M., Coffin, S., Cole, M., Hermabessiere, L., Koelmans, A.A., Rochman, C.M., 2022. Characterizing microplastic hazards: which concentration metrics and particle characteristics are most informative for understanding toxicity in aquatic organisms? Micropl.&Nanopl. 2, 20. https://doi.org/10.1186/s43591-022-00040-4

Thuan, P.M., Nguyen, M.-K., Nguyen, D.D., 2025. The potential release of microplastics from paint fragments: Characterizing sources, occurrence and ecological impacts. Environ Geochem Health 47. https://doi.org/10.1007/s10653-025-02525-6

Weber, C.J., Kundel, D., Fliessbach, A., Bünemann, E.K., Bigalke, M., 2025. Baseline levels of microplastics in agricultural soils obscure the effects of additional microplastics from recycled fertilizers. Microplastics and Nanoplastics 5, 30. https://doi.org/10.1186/s43591-025-00136-7

Wu, X., Gu, W., Peng, S., Bai, J., 2025. Investigating the distribution of microplastics in soils from e-waste dismantling sites and their adsorption of heavy metals. Waste Manag Res 43, 386–396. https://doi.org/10.1177/0734242X241251432

Xiao, X., He, E., Jiang, X., Li, X., Yang, W., Ruan, J., Zhao, C., Qiu, R., Tang, Y., 2022. Visualizing and assessing the size-dependent oral uptake, tissue distribution, and detrimental effect of polystyrene microplastics in *Eisenia fetida*. Environmental Pollution 306, 119436. https://doi.org/10.1016/j.envpol.2022.119436

Xu, L., Li, J., Yang, S., Li, Z., Liu, Y., Zhao, Y., Liu, D., Créso Targino, A., Zheng, Z., Yu, M., Xu, P., Sun, Y., Li, W., 2024. Characterization of atmospheric microplastics in Hangzhou, a megacity of the Yangtze river delta, China. Environ. Sci.: Atmos. 4, 1161–1169. https://doi.org/10.1039/D4EA00069B

Xu, Q., Gao, Y., Xu, L., Shi, W., Wang, F., LeBlanc, G.A., Cui, S., An, L., Lei, K., 2020. Investigation of the microplastics profile in sludge from China's largest Water reclamation plant using a feasible isolation device. Journal of Hazardous Materials 388, 122067. https://doi.org/10.1016/j.jhazmat.2020.122067

5 Supplementary material

Figures

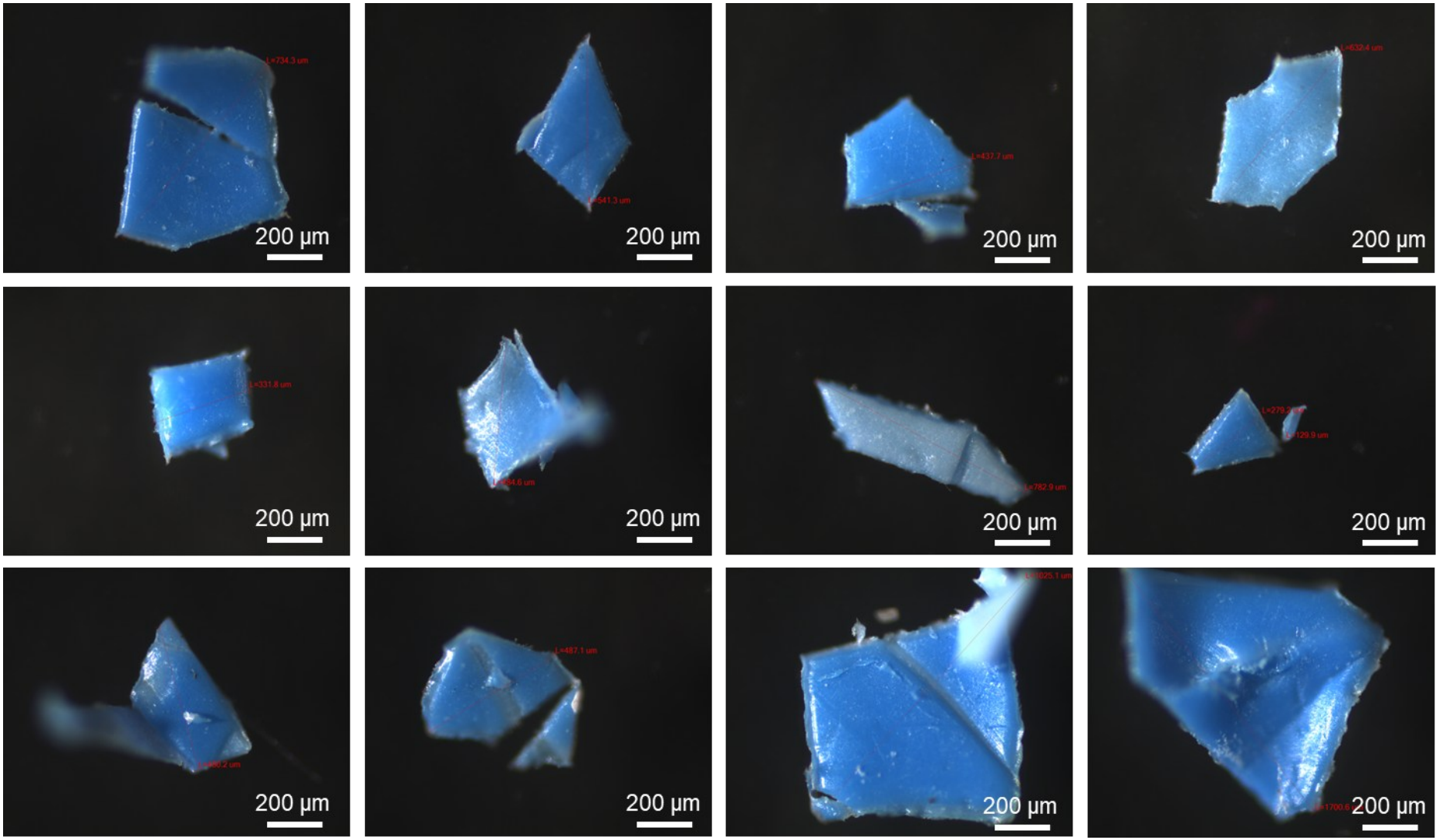

Figure S1. Particles of blue PE before the pretreatment in control 1. Figure from Bertoldi et al. (2026).

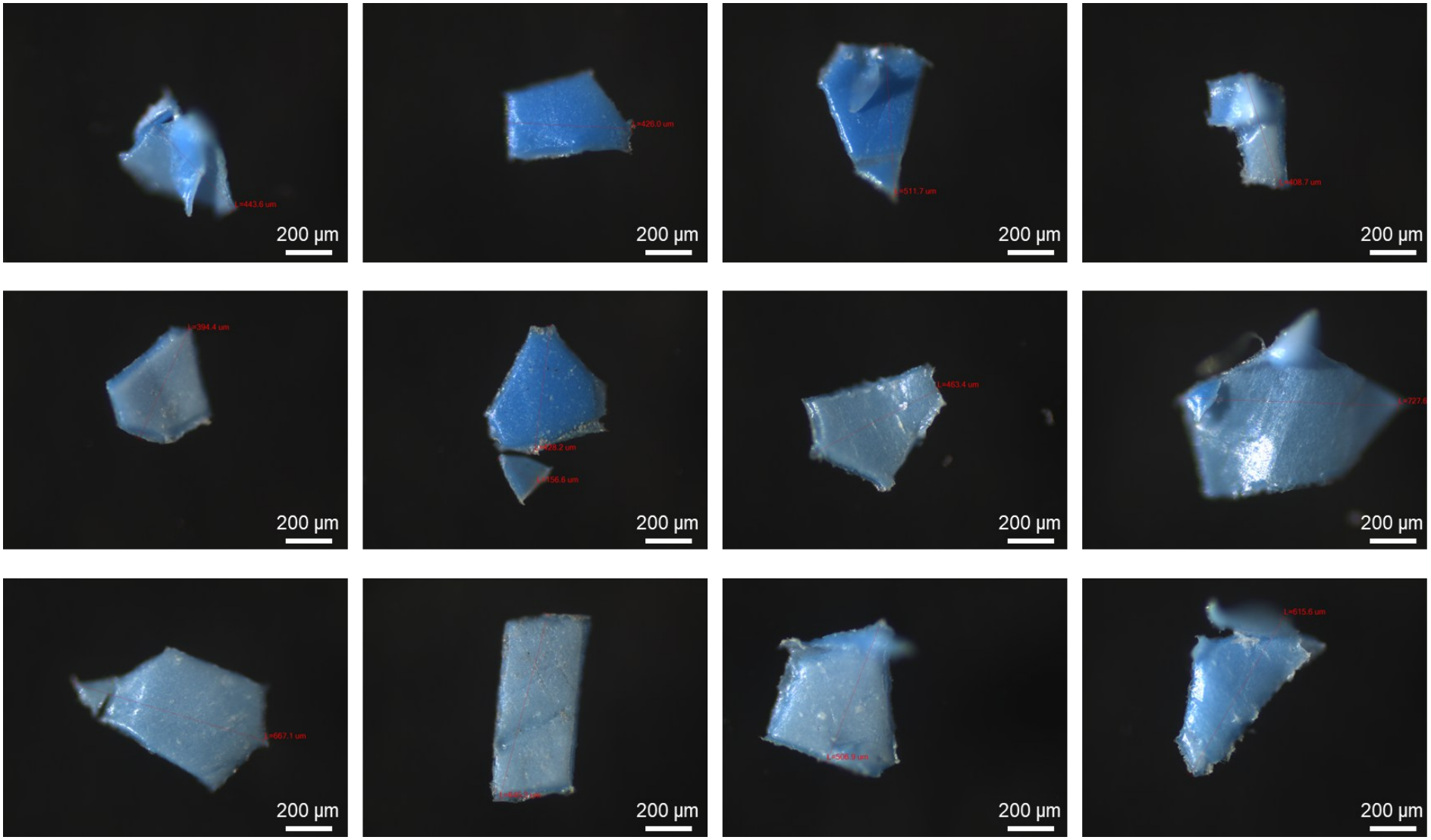

Figure S2. Particles of blue PE before the pretreatment in control 2. Figure from Bertoldi et al. (2026).

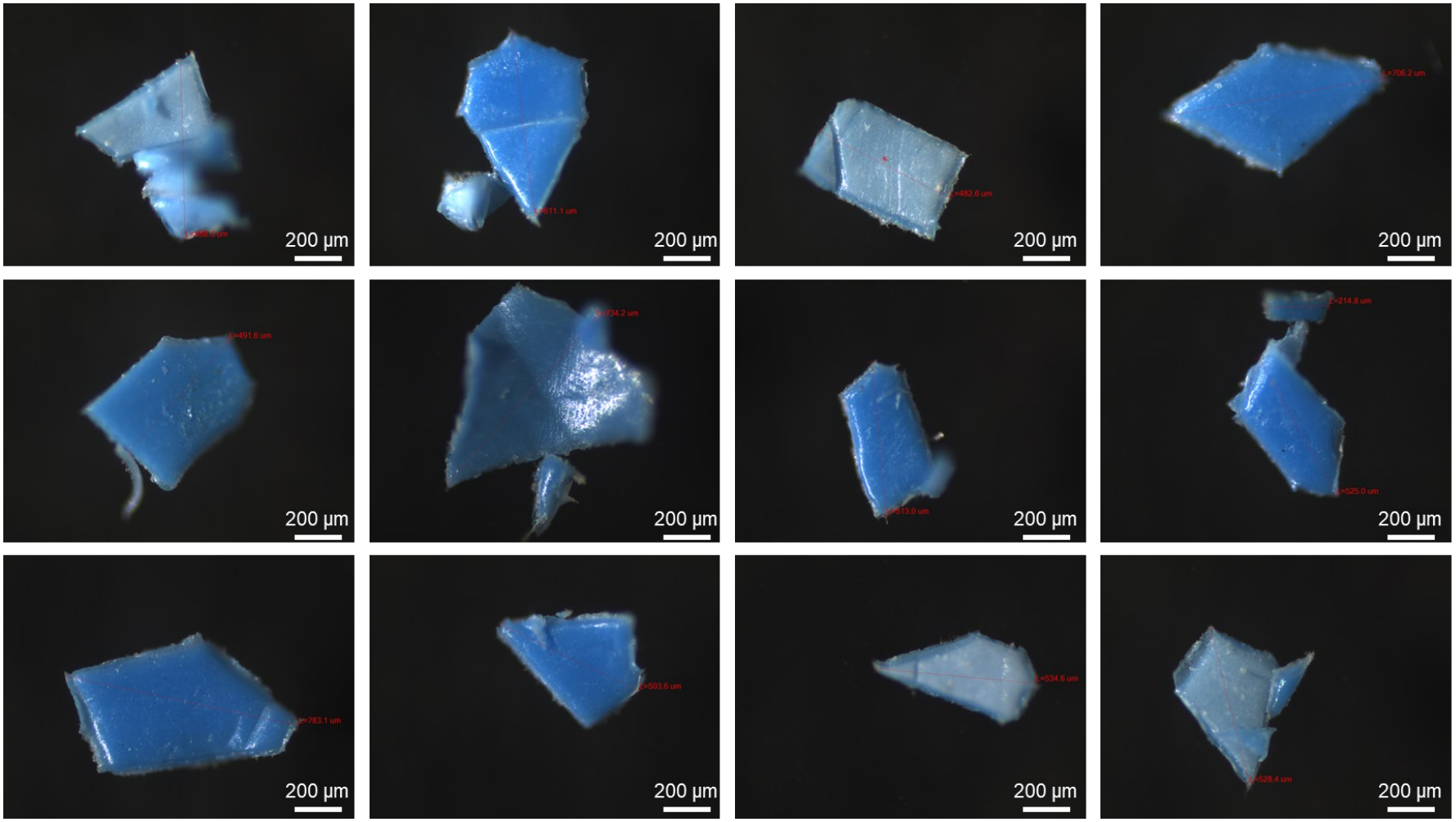

Figure S3. Particles of blue PE before the pretreatment in control 3. Figure from Bertoldi et al. (2026).

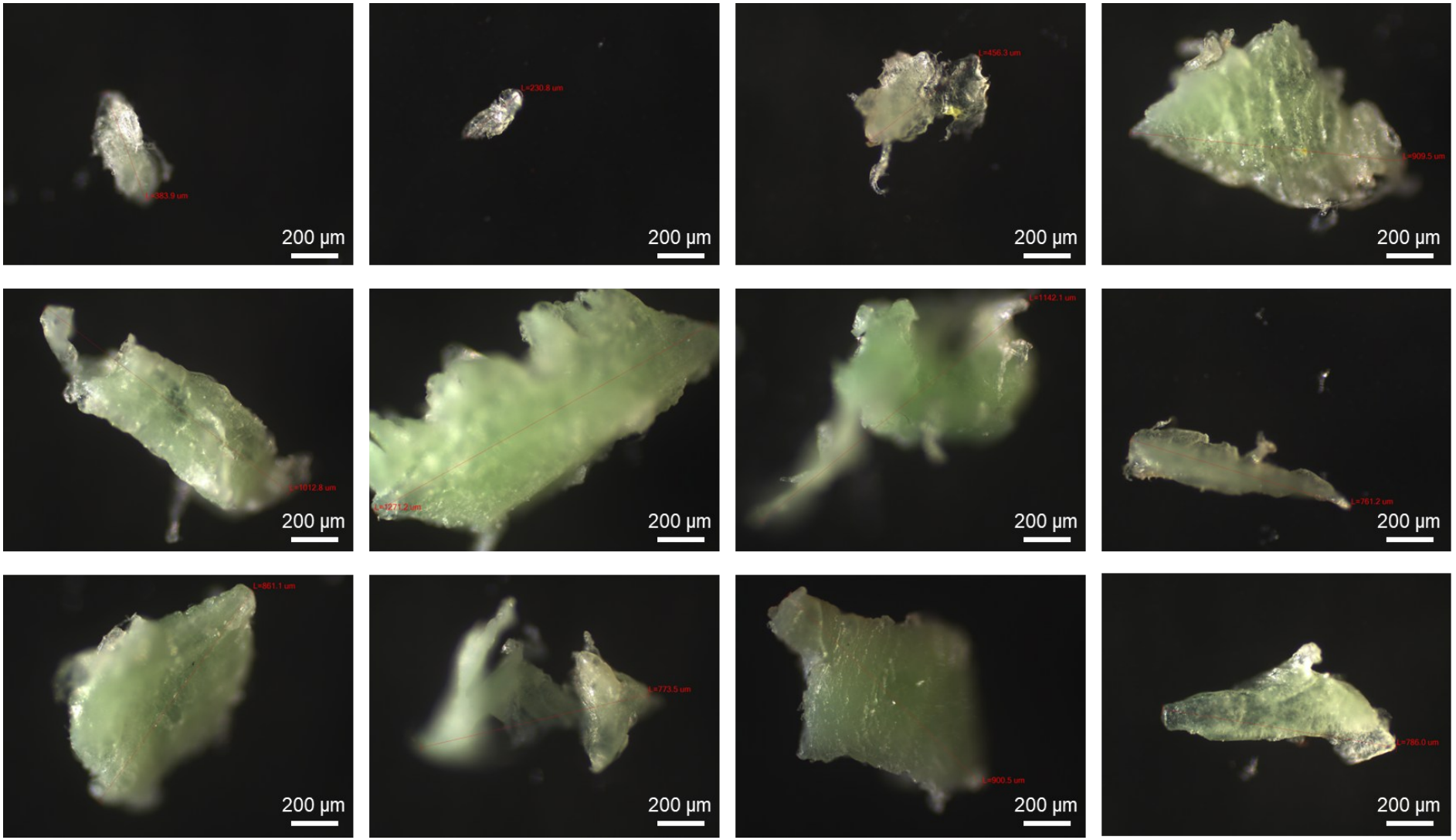

Figure S4. Particles of blue PP before the pretreatment in control 1. Figure from Bertoldi et al. (2026).

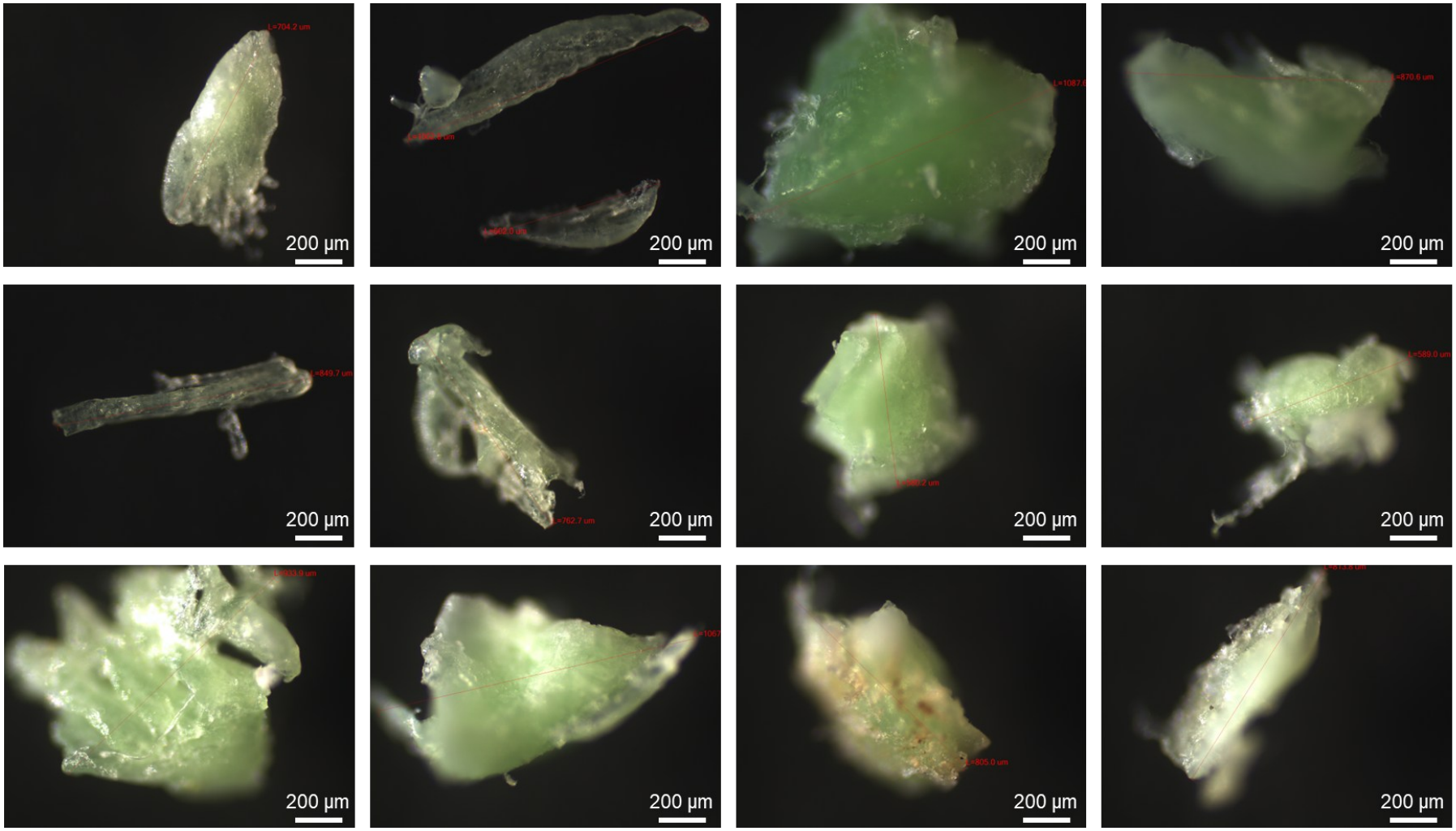

Figure S5. Particles of blue PP before the pretreatment in control 2. Figure from Bertoldi et al. (2026).

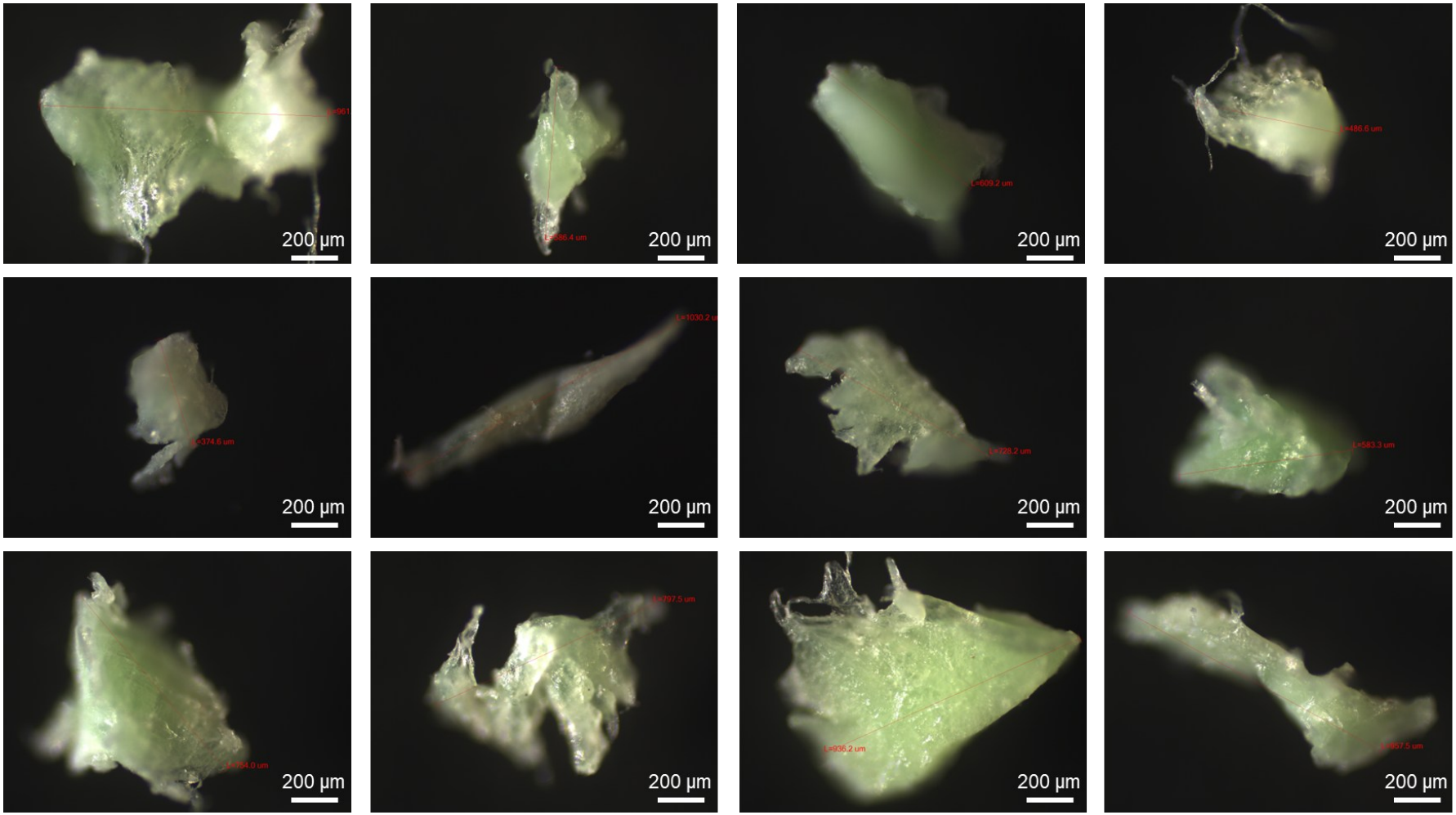

Figure S6. Particles of blue PE before the pretreatment in control 3. Figure from Bertoldi et al. (2026).

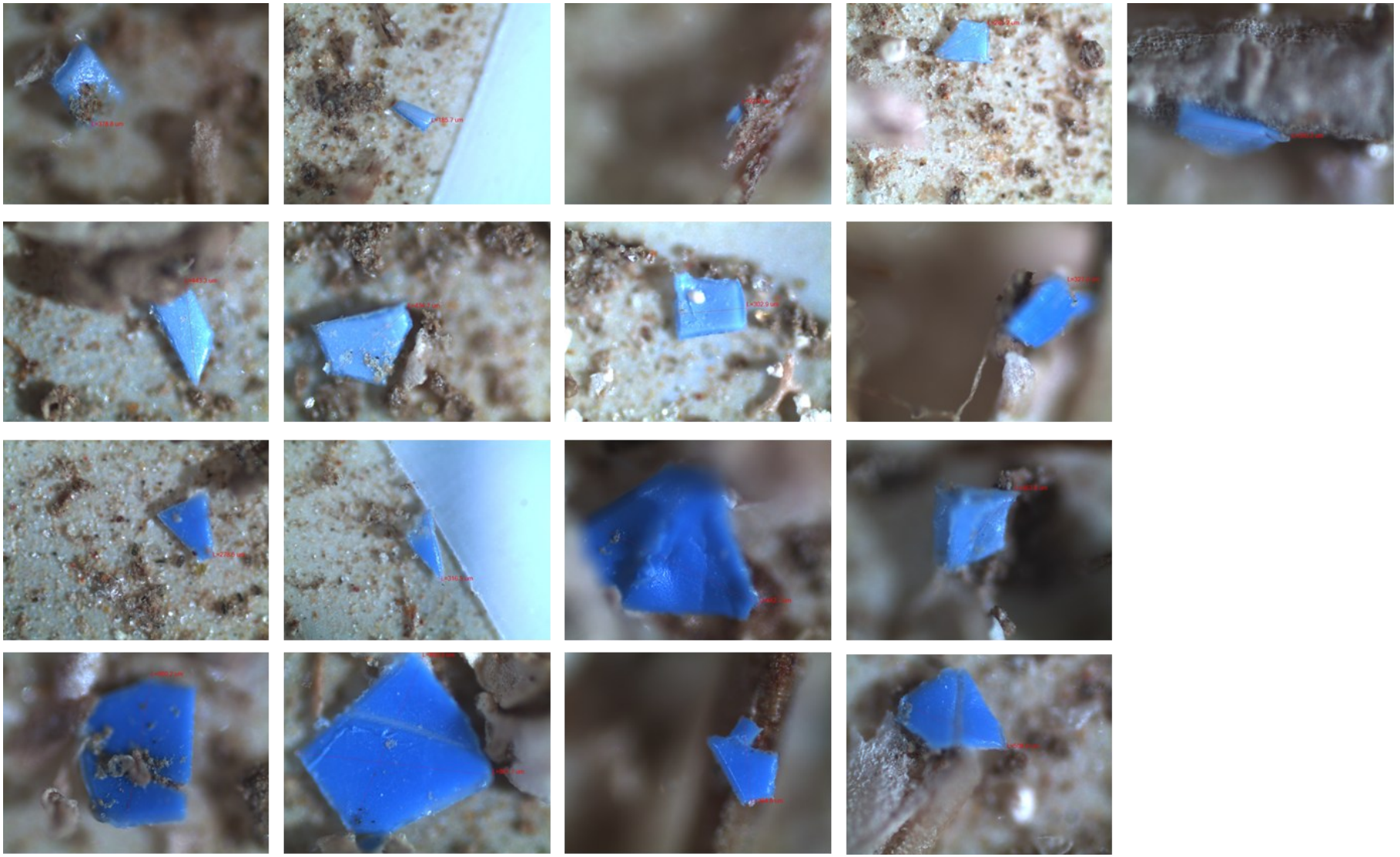

Figure S7. Particles of blue PE after the pretreatment in control 1. Figure from Bertoldi et al. (2026).

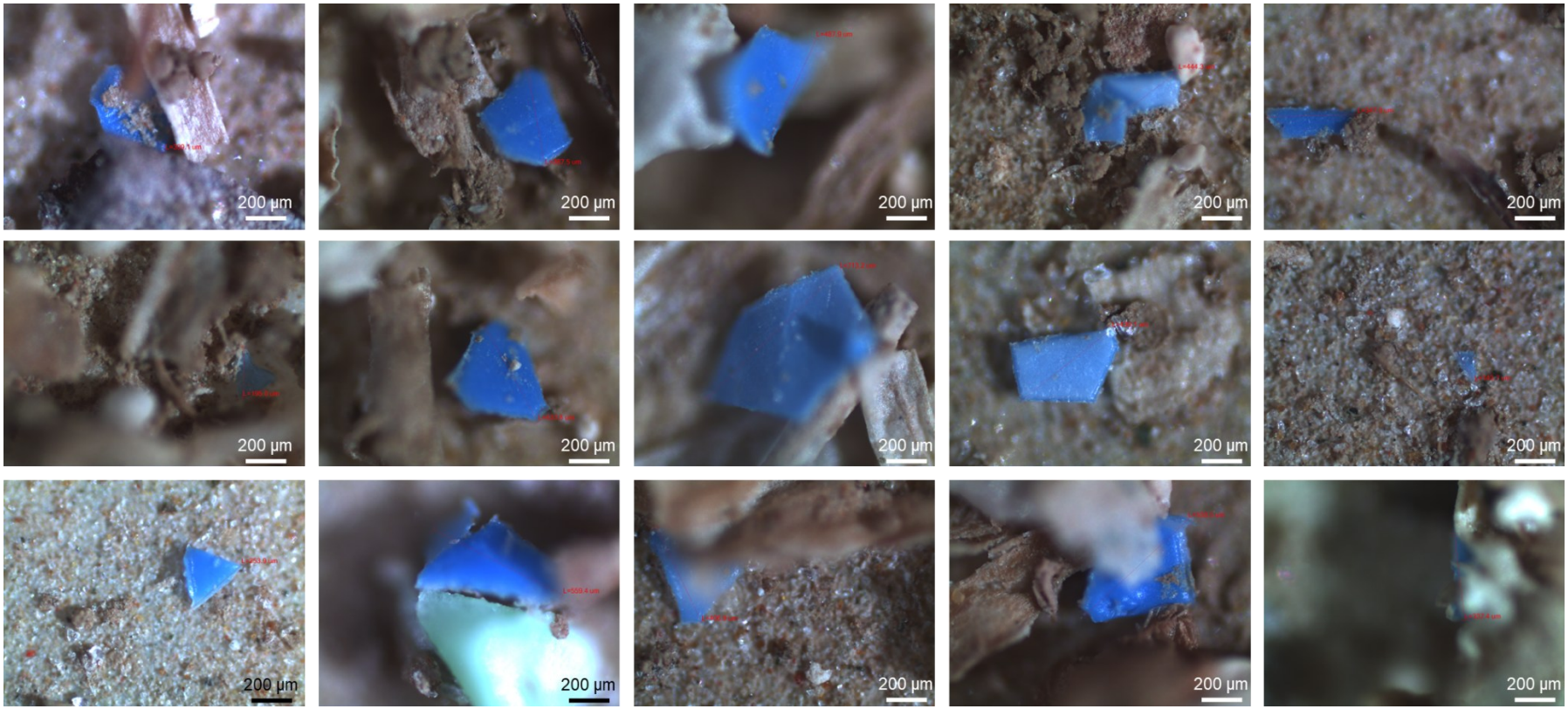

Figure S8. Particles of blue PE after the pretreatment in control 2. Figure from Bertoldi et al. (2026).

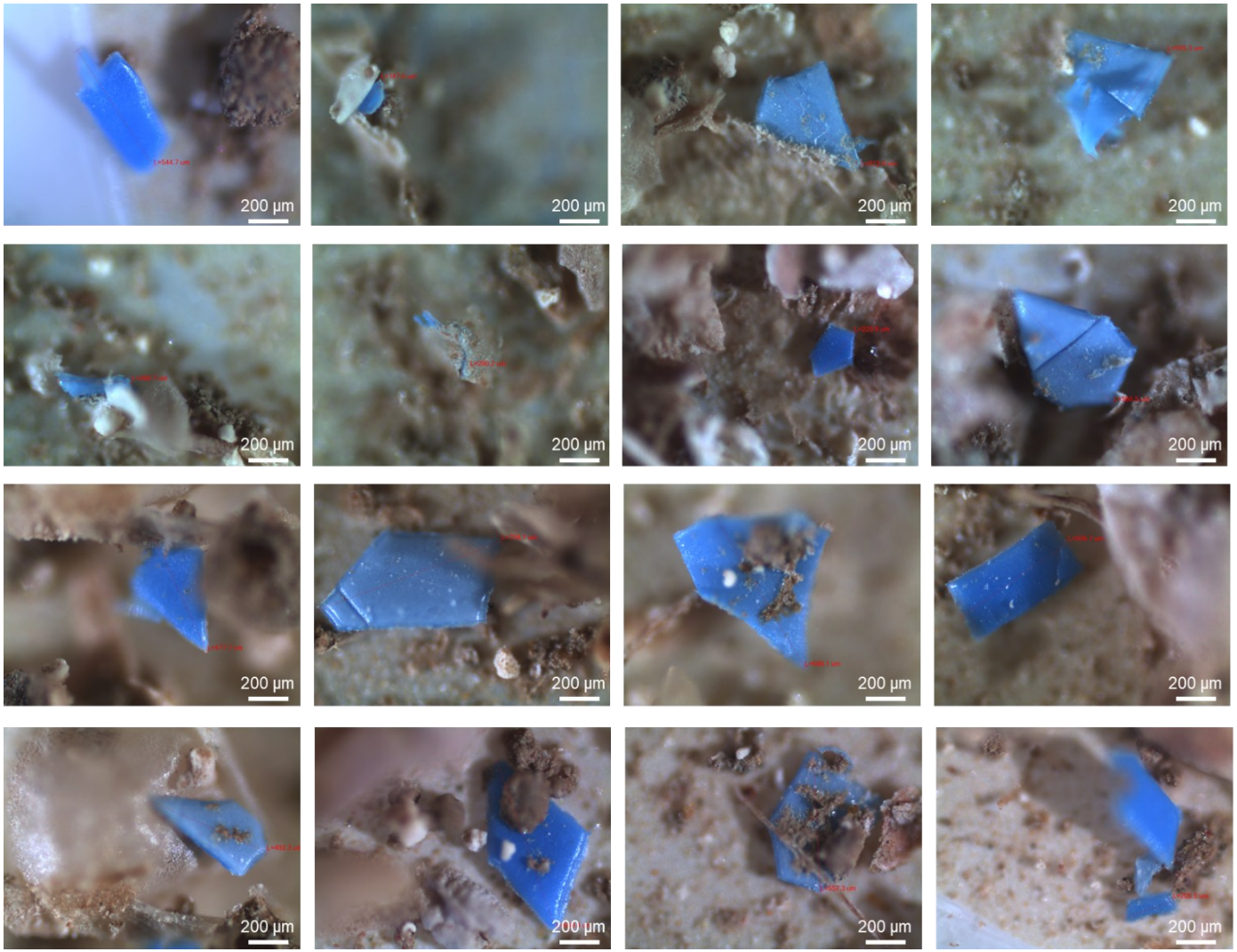

Figure S9. Particles of blue PE after the pretreatment in control 3. Figure from Bertoldi et al. (2026).

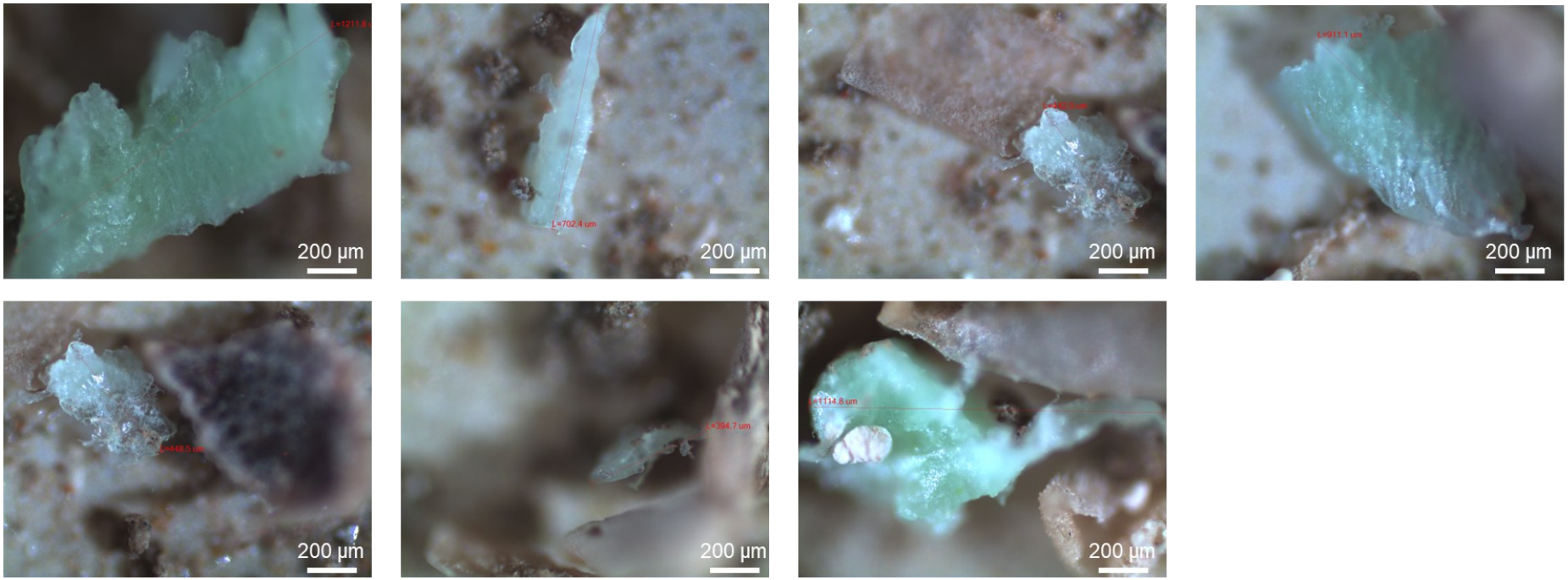

Figure S10. Particles of blue PP after the pretreatment in control 1. Figure from Bertoldi et al. (2026).

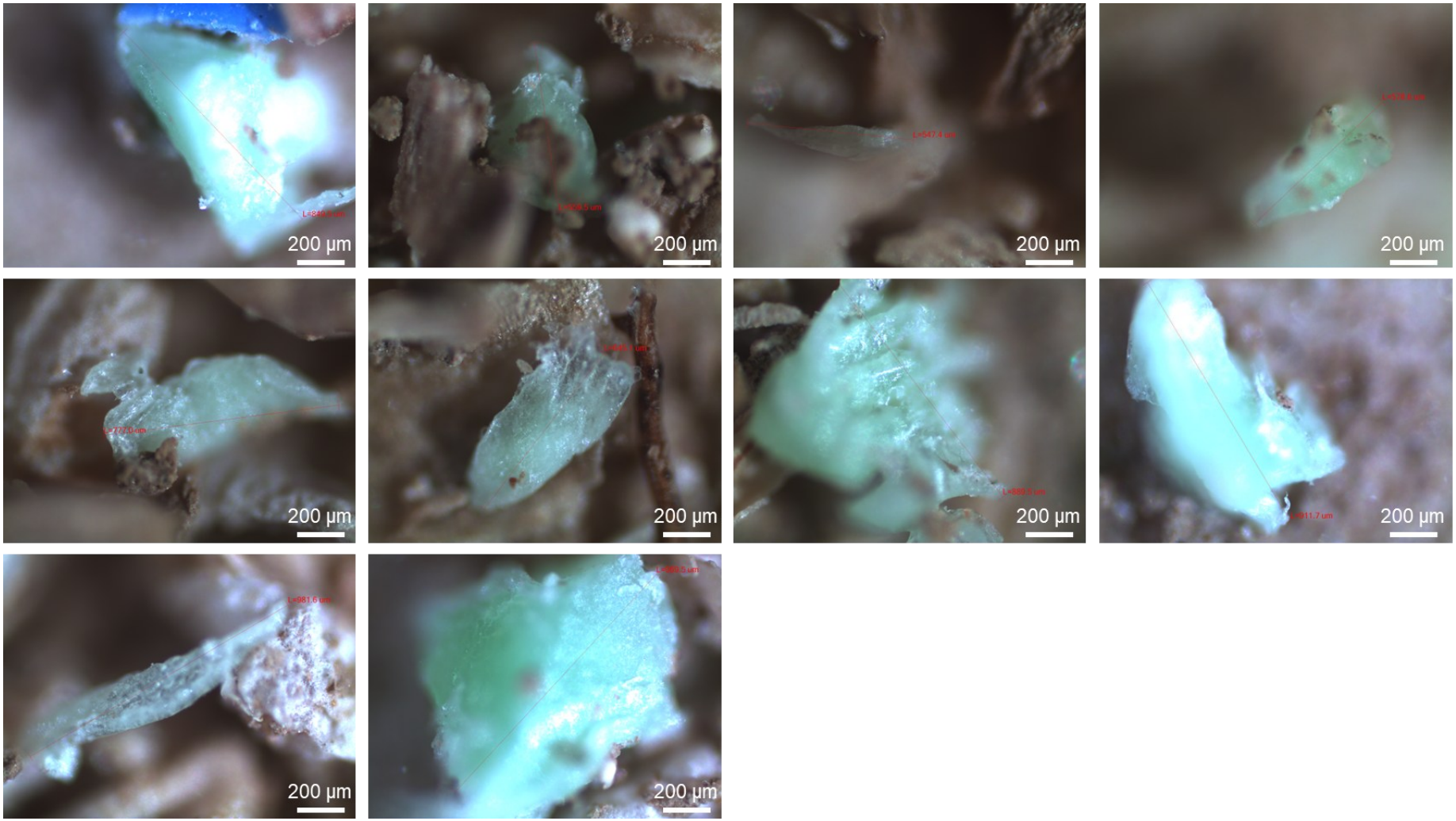

Figure S11. Particles of blue PP after the pretreatment in control 2. Figure from Bertoldi et al. (2026).

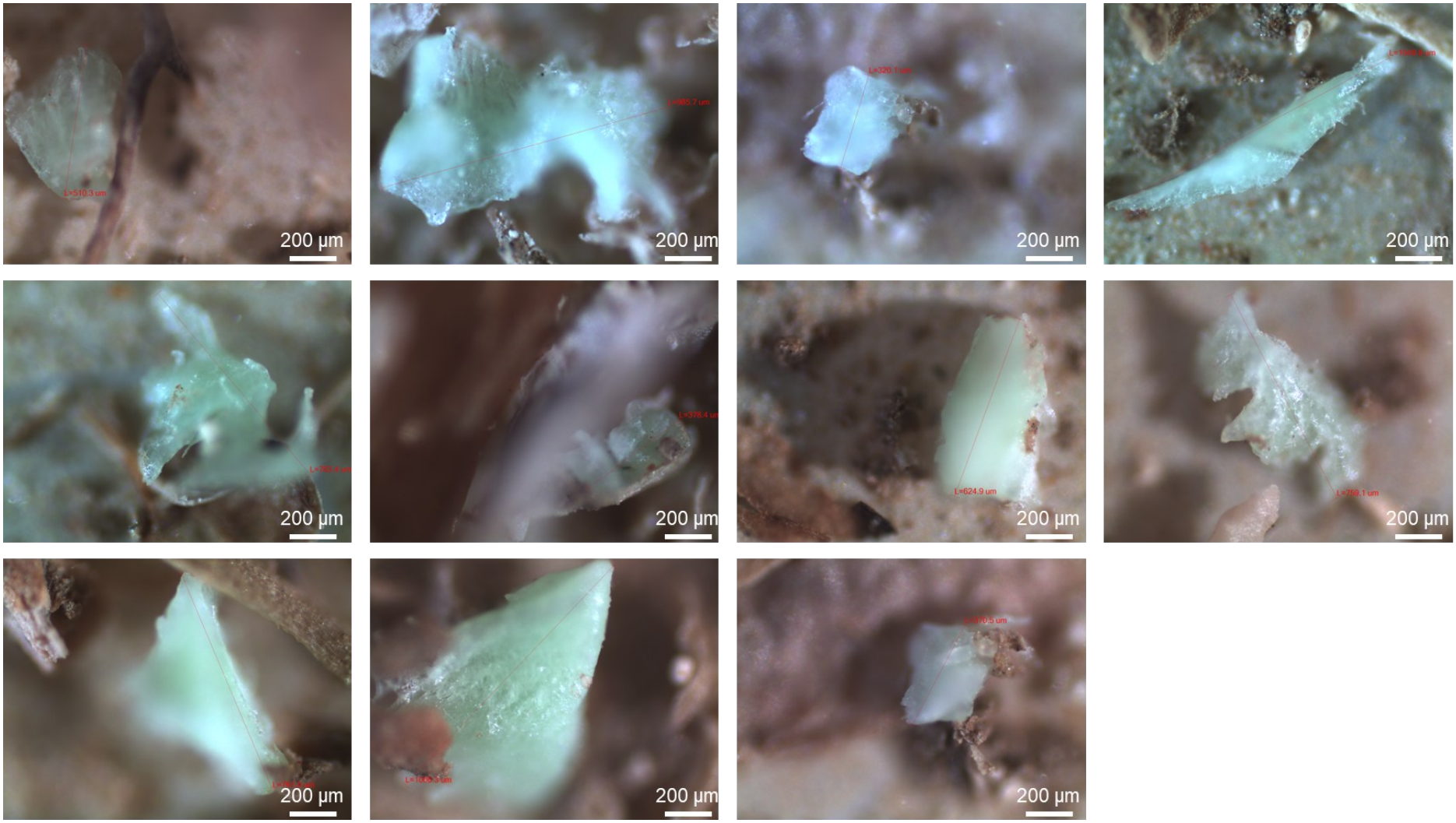

Figure S12. Particles of blue PE after the pretreatment in control 3. Figure from Bertoldi et al. (2026).

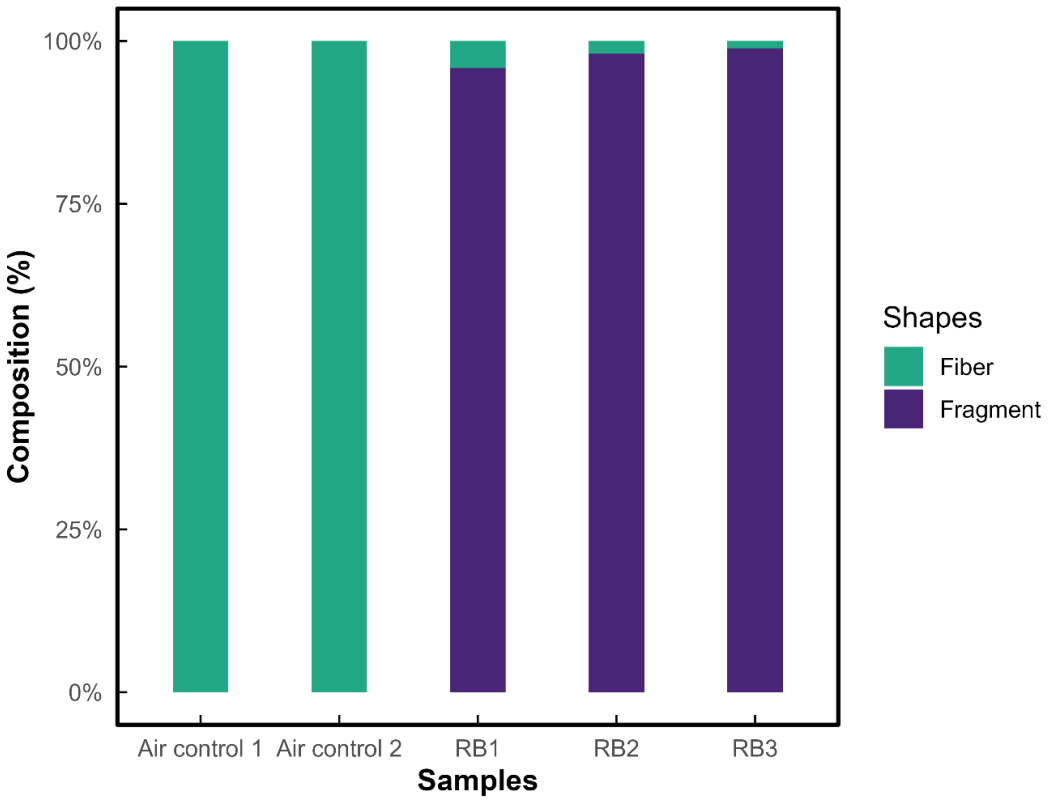

Figure S13. Shape composition by sample. Bars are normalized to 100% per sample. Across all combined samples, 2,372 particles were quantified, with fragments 98.0% (n = 2,325) and fibers 2.0% (n = 47). No error bars are shown because values represent the full set of counted particles. Figure from Bertoldi et al. (2026).

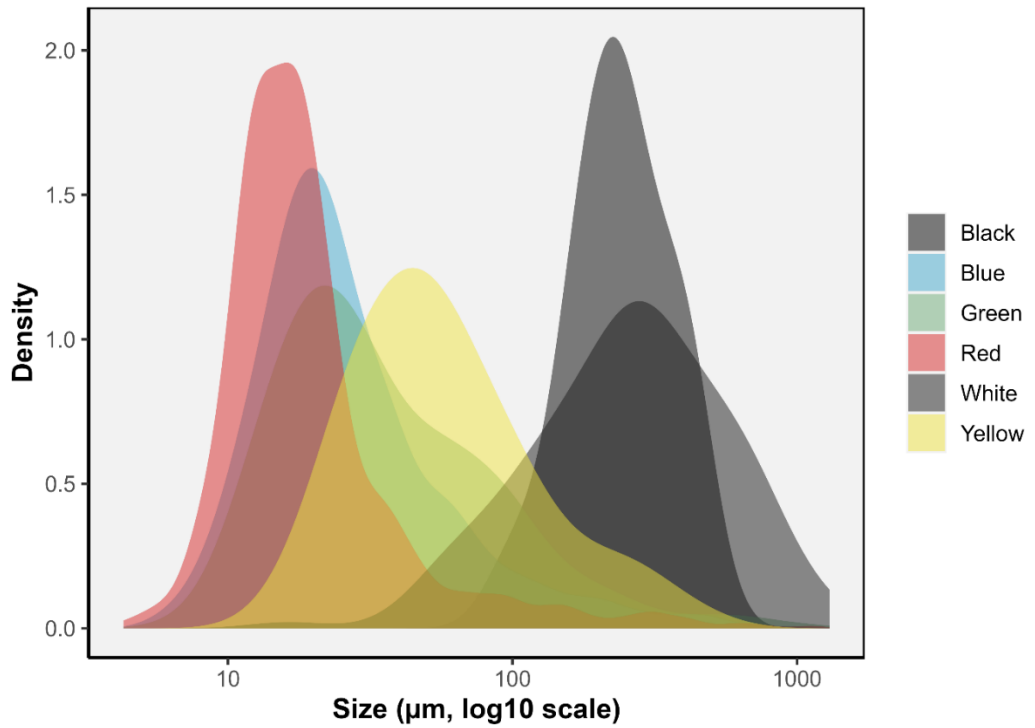

Figure S14. Density distribution of colors in the biofertilizer samples. The distribution exclude fibers due to their low number. Figure from Bertoldi et al. (2026).

Tables

Table S1. Sizes of the PE and PP particles before and after the extraction process.

Control 1				Control 2				Control 3			
PE		PP		PE		PP		PE		PP	
Before	After	Before	After	Before	After	Before	After	Before	After	Before	After
734.3	378.8	383.9	1211.8	443.6	399.1	704.2	849.5	588.3	205.5	961	510.3
541.3	185.7	230.8	702	426	387.5	1062.6	559.5	611.1	544.7	586.4	985.7
437.7	92.8	456.3	442	511.7	487.5	602	547.4	482.6	147	609.2	320.1
632.4	261.2	909.5	911.1	408.7	444.3	1087.6	777	706.2	512	486.6	1049.8
331.8	500.2	1012.8	448.5	394.4	347	870.6	645	491.6	505.3	374.6	783.4
484.6	443.3	1271.2	394.7	428.2	195	849.7	880.5	734.2	492.3	1030.2	378.4
782.9	434.7	1142	1148.8	156	433.8	762.7	911.7	513	288.7	782.2	624.9
279.2	302.9	761.2		463.4	715.2	580.2	981.6	525	280.2	583.3	759.1
129.2	327.2	861.1		727	439.1	589	969.5	783.1	229.9	754	781
480.2	278.5	773.5		667.1	143.7	933.9	578.6	503.6	586.5	797.5	1006.3
487.1	316.5	900.5		645.3	253.9	1067		534.6	699.4	936.2	370.3
1025.1	660.2	786		506.9	559.4	805		528.4	477.7	957.2	
1700.6	861.7			615.6	406.9	813.8			759.1		
	842.7				530.5				689.1		
	463.8				337.4				506.7		
	384.6								557.3		
	508.4										

Table from Bertoldi et al. (2026).

Table S2. Composition of particle shapes across samples and air controls.

Samples	Fiber	Fragment
Air control 1	N=25 (100%)	N=0 (0%)
Air control 2	N=14 (100%)	N=0 (0%)
RB1	N=14 (4.1%)	N=328 (95.9%)
RB2	N=25 (1.9%)	N=1291 (98.1%)
RB3	N=8 (1.1%)	N=706 (98.9%)

Table from Bertoldi et al. (2026).

Table S3. Pairwise Wilcoxon tests for fragment size by color. HL = Hodges–Lehmann median difference (group1 − group2). P-values are Benjamini–Hochberg adjusted across all pairs. Positive HL indicates group 1 larger. Medians µm.

Groups	n1	n2	median1	median2	HL_diff_CI	p_BH
Red vs White	885	138	16.8	269	-246.4 [-263.3, -223.4]	$3.60E^{-71}$
Blue vs White	678	138	22.6	269	-235.7 [-256.0, -208.5]	$4.58E^{-65}$
Green vs White	552	138	29.1	269	-223.0 [-247.0, -195.7]	$7.95E^{-57}$
Green vs Red	552	885	29.1	16.8	11.2 [9.5, 13.1]	$7.79E^{-51}$
Blue vs Red	678	885	22.6	16.8	5.5 [4.5, 6.5]	$2.46E^{-25}$
Red vs Yellow	885	55	16.8	51.8	-31.8 [-38.1, -25.3]	$2.87E^{-22}$
White vs Yellow	138	55	269	51.8	200.9 [156.7, 243.4]	$1.57E^{-18}$
Blue vs Yellow	678	55	22.6	51.8	-24.6 [-32.0, -17.6]	$7.15E^{-13}$
Black vs Red	17	885	233.4	16.8	212.5 [183.9, 246.8]	$1.65E^{-11}$
Black vs Blue	17	678	233.4	22.6	204.3 [171.5, 240.6]	$3.51E^{-11}$
Black vs Green	17	552	233.4	29.1	194.8 [159.3, 231.8]	$1.41E^{-10}$
Blue vs Green	678	552	22.6	29.1	-5.6 [-7.6, -3.7]	$1.86E^{-09}$
Black vs Yellow	17	55	233.4	51.8	173.2 [135.6, 214.5]	$7.27E^{-08}$
Green vs Yellow	552	55	29.1	51.8	-17.2 [-25.4, -10.2]	$5.37E^{-06}$
Black vs White	17	138	233.4	269	-24.4 [-112.2, 50.1]	0.519

Table S4. Descriptive statistics of fragment sizes (µm) by colors.

Colors	n	Mean	SD	Median	Min	Max
Red	885	31	68.9	16.8	4.3	1117.9
Blue	678	41.9	69.7	22.6	5.6	919.5
Green	552	59.3	99.5	29.1	6.6	1088
White	138	331	242.6	269	16.3	1300
Yellow	55	77.3	76.2	51.8	17	417.2
Black	17	256.5	99.6	233.4	100.8	448.5

Table from Bertoldi et al. (2026).

Table S5. Color differences in proportions across samples. Chi-square Benjamini–Hochberg false discovery rate (BH–FDR) q-values. Table from Bertoldi et al. (2026).

Color	RB1 (%)	RB2 (%)	RB3 (%)	p_value	q_value
green	25.4	20.8	26.8	0.006199	0.020561
white	6.4	7.8	4.2	0.006854	0.020561
yellow	4.1	2.3	1.8	0.071174	0.142348
black	2.3	1.4	1.1	0.303753	0.433152
blue	26.3	29.8	27.7	0.36096	0.433152

red	35.4	37.8	38.4	0.627715	0.627715

Table S6. Pairwise differences in color proportions between samples (RB1–RB3). Chi-square test with BH-FDR q-values.

Color	Pair	Pair 1	Pair 2	p_value	q_value
white	RB2 vs RB3	7.8	4.2	0.001622	0.021578
green	RB2 vs RB3	20.8	26.8	0.002398	0.021578
yellow	RB1 vs RB3	4.1	1.8	0.02855	0.171301
yellow	RB1 vs RB2	4.1	2.3	0.062968	0.234891
green	RB1 vs RB2	25.4	20.8	0.065248	0.234891
white	RB1 vs RB3	6.4	4.2	0.116888	0.332308
black	RB1 vs RB3	2.3	1.1	0.129231	0.332308
blue	RB1 vs RB2	26.3	29.8	0.207831	0.467619
black	RB1 vs RB2	2.3	1.4	0.243778	0.487557
blue	RB2 vs RB3	29.8	27.7	0.329932	0.556217
red	RB1 vs RB3	35.4	38.4	0.346554	0.556217
white	RB1 vs RB2	6.4	7.8	0.384355	0.556217
red	RB1 vs RB2	35.4	37.8	0.401712	0.556217
yellow	RB2 vs RB3	2.3	1.8	0.49292	0.633754
black	RB2 vs RB3	1.4	1.1	0.543714	0.652457
blue	RB1 vs RB3	26.3	27.7	0.628922	0.688775
green	RB1 vs RB3	25.4	26.8	0.65051	0.688775
red	RB2 vs RB3	37.8	38.4	0.813128	0.813128

Table from Bertoldi et al. (2026).

Table S7. Descriptive statistics of fragment sizes by sample (original scale). FRAGMENT

Samples	n	min	Median	Mean	max	sd
RB1	328	6.8	28.5	70.1	919.5	118.5
RB2	1290	5.2	22.0	62.8	1300.0	123.0
RB3	706	5.2	20.0	52.3	1248.3	106.1

Table from Bertoldi et al. (2026).

Table S8. Pairwise comparisons of fragment-size distributions across samples RB1–RB3. Cramér–von Mises (CvM) tests with FDR-adjusted q-values and Vargha–Delaney A12 effect sizes for pairwise sample comparisons of particle sizes.

Pair	CvM	q (FDR)	A12	Magnitude	Direction
RB1 x RB2	12.71	$7.50e^{-5}$	0.577	Small	RB1>RB2
RB1 x RB3	18.69	$7.50e^{-5}$	0.621	Small	RB1>RB3
RB2 x RB3	4.83	$1.90e^{-3}$	0.544	Negligible	RB2>RB3

q values are Benjamini–Hochberg FDR-adjusted p-values (permutation CvM). A12 magnitudes use Vargha–Delaney cutoffs: negligible <0.56, small 0.56–0.64, medium 0.64–0.71, large ≥0.71. Direction reports which sample tends larger (e.g., RB1 > RB3).
Table from Bertoldi et al. (2026).

Table S9. Polymer composition (%) in percentage across the samples.

Polymers	RB1	RB2	RB3	Average	SD
NI	32	35	20	29	8
Paint-based	30	18	21	23	6
PE	9	11	17	12	4
PS	8	9	10	9	1
PP	6	7	9	7	1
PU	4	5	7	6	2
PES	4	2	3	3	1
Rubber	1	3	4	2	2
PMMA	2	3	1	2	1
PET	1	3	3	2	1
ABS	1	1	2	1	1
PVC	0	2	1	1	1
Acrylic	1	1	0	1	0
Cotton	1	0	0	0	0
EVA	1	0	0	0	0
Nylon	0	0	1	0	1
PEA	1	0	0	0	0
PEVA	0	0	0	0	0
Cellulose	0	0	0	0	0
PA	0	0	0	0	0

PE (polyethylene); PS (polystyrene); PP (polypropylene); PU (polyurethane); PES (polyester); Rubber; PMMA (poly(methyl methacrylate)); PET (poly(ethylene terephthalate)); ABS (acrylonitrile–butadiene–styrene); PVC (poly(vinyl chloride)); Acrylic; Cotton; EVA (ethylene–vinyl acetate).
Table from Bertoldi et al. (2026).

Table S2. Feret's diameter and area of selected particles used to mass estimations. The measurements were performed with software package ImageJ (version 1.54d).

Maximum Feret diameter (µm)	Area (µm^2)
67	2344
78	3002
20.2	217
28.9	521
12.4	34
19.7	86
8	16
18.1	78
11.4	24
12.7	121

Table S3. Theoretical mass estimation of microplastics in the biofertilizer samples.

Sample	mg MPs kg^{-1}	g MPs ha^{-1}*	g MPs ha^{-1}**	Total input (Kg yr^{-1})
RB1	0.05± 0.01	1.9±0.28	2.7±0.40	111±14
RB2	0.19 ± 0.02	6.9±0.86	9.9±1.22	393±42
RB3	0.13 ± 0.10	6.8±1.59	9.7±2.27	381±78

*Estimation performed considering phosphorous concentration in RB1 (0.60g Kg^{-1})
**Estimation performed considering phosphorous concentration in RB2 (0.42g Kg^{-1})
Table from Bertoldi et al. (2026).

Table S5. Descriptive statistics for fiber size (μm) in samples and air controls: N, mean (SD), median, minimum, and maximum.

Group	N	Mean	SD	Median	Min	Max
Control	39	628	363	600	72.5	1445
Samples	47	436	319	390	16.6	1223

Table from Bertoldi et al. (2026).